Nonequilibrium dynamics of spin glasses: Examination of the ghost domain scenario

P. E. Jönsson,* R. Mathieu,† and P. Nordblad
Department of Materials Science, Uppsala University, Box 534, SE-751 21 Uppsala, Sweden

H. Yoshino
Department of Earth and Space Science, Faculty of Science, Osaka University, Toyonaka, 560-0043 Osaka, Japan

H. Aruga Katori and A. Ito
RIKEN, Hirosawa 2-1, Wako, Saitama, 351-0198, Japan

(Received 25 July 2003; revised manuscript received 6 July 2004; published 3 November 2004)

Extensive experimental and numerical studies of the nonequilibrium dynamics of spin glasses subjected to temperature or bond perturbations have been performed to investigate chaos and memory effects in selected spin-glass systems. Temperature shift and cycling experiments were performed on the strongly anisotropic Ising-like system $Fe_{0.5}Mn_{0.5}TiO_3$ and the weakly anisotropic Heisenberg-like system Ag(11 at% Mn), while bond shift and cycling simulations were carried out on a four-dimensional Ising Edwards-Anderson spin glass. These spin-glass systems display qualitatively the same characteristic features, and the observed memory phenomena are found to be consistent with predictions from the ghost-domain scenario of the droplet scaling model.

DOI: 10.1103/PhysRevB.70.174402 PACS number(s): 75.10.Nr, 75.40.Gb, 75.50.Lk

I. INTRODUCTION

Spin glasses (SG) have been an active field of research for the last three decades. Experimental and theoretical studies have revealed an unexpected complexity to a deceivingly simple problem formulation.[1–3] Many open questions still remain, not the least concerning the nonequilibrium dynamics of the spin-glass phase.[4,5] Aging,[6] rejuvenation, and memory[7,8] are intriguing characteristics of the nonequilibrium dynamics in spin glasses. Similar features are to a certain extent found also in other glassy systems, such as orientational glasses,[9] polymers,[10] strongly interacting nanoparticle systems,[11,12] colossal magnetoresistive manganites,[13] and certain ceramic superconductors.[14,15]

Aging itself can be found in much simpler systems, such as standard phase-separating systems. An example is a mixture of oil and vinegar used in salad dressing. By strongly shaking the mixture the system can be rejuvenated and slow growth of equilibrium domains of oil and vinegar is observed afterward. Then the first nontrivial question is what is growing in glassy systems during aging. Moreover the aging observed in spin glasses is very unusual in several respects. First, the spin-glass system can be strongly rejuvenated by an extremely weak perturbation, such as a small change of temperature. Second, memory effects can be observed even after such strong rejuvenation. These two aspects are in sharp contrast to the aging in simpler systems. In the case of the oil-and-vinegar system, one has to shake the mixture strongly to rejuvenate it and such a strong rejuvenation will completely eliminate memories of the original mixture.

A natural physical picture for the aging, rejuvenation, and memory effects in spin glasses are proposed by the droplet picture[16–19] and its recent extension—the ghost domain scenario.[20–22] This picture includes concepts, such as aging by domain growth, rejuvenation by chaos with temperature or bond changes, and memory by ghost domains.

The purpose of this study is to find out how chaos effects are reflected on the nonequilibrium dynamics and to which extent they are relevant for spin glasses within the available time window. It has been proposed in several recent papers[23–26] that the memory effects observed in experiments can be understood without the concept of temperature chaos, but simply as due to successive freezing of smaller and smaller length scales on cooling, in other words, as the classical Kovacs effect[27] observed in many glassy systems. The experiments and simulations reported in this paper are inspired by and inherit protocols, methods, and ideas from Refs. 20–22 and 28–30. Our approach allows us to distinguish between the classical Kovacs effect and rejuvenation-memory effects due to temperature chaos.

This article is organized as follows: In Sec. II we discuss the consequences of chaotic perturbations (temperature or bond changes) on the nonequilibrium dynamics of spin glasses based on the ghost domain scenario. A special emphasis is put on how spin glasses that have been subjected to a strong perturbation gradually recover their original spin structure. A brief introduction to experiments and simulations is given in Sec. III. Section IV is devoted to results from detailed temperature-shift experiments on the $Fe_{0.5}Mn_{0.5}TiO_3$ and Ag(11 at% Mn) samples and bond-shift simulations on the four-dimensional (4D) Edwards-Anderson (EA) spin glass. Rejuvenation effects after perturbations of various strengths are investigated in detail. Section V concerns one- and two-step temperature cycling experiments on the Ag(11 at% Mn) sample as well as bond cyclings on the four-dimensional EA model. The interest is the recovery of memory after various perturbations. In Sec. VI, results from new memory experiments on $Fe_{0.5}Mn_{0.5}TiO_3$ and Ag(11 at% Mn) samples are reported and the influence of cooling and heating rate effects are discussed.

II. THEORY

In this section we present the theoretical basis for our experimental and numerical studies on the dynamics of spin glasses and related randomly frustrated systems subjected to perturbations, such as temperature (T) shifts/cyclings and bond shifts/cyclings.

One major basis is the prediction of strong rejuvenation due to the so-called chaos effects originally found within the droplet, domain-wall scaling theory due to Bray-Moore and Fisher-Huse.[16–19] This theory predicts that spin glasses are very sensitive to changes in their environments. Even an infinitesimal change of temperature or, equivalently, an infinitesimal change of the bonds will reorganize the spin configuration toward completely different equilibrium states. The existence of the anticipated chaos effects in the bulk properties of certain glassy systems have been confirmed by some theoretical and numerical studies, e.g., on the Edwards-Anderson Ising spin-glass models using the Migdal-Kadanoff renormalization group method[21,31–33] and the mean-field theory[34] as well as on directed polymers in random media.[35] However, numerical simulations on the EA models on "realistic" lattices, such as the three-dimensional (3D) cubic lattice, remain inconclusive about the existence of the temperature-chaos effect due to the lack of computational power.[36–41] Furthermore, the link between the chaos effect and the rejuvenation effect observed in experiments remains to be clarified. It has been argued that the chaos effect, even if it exists, may be irrelevant at the length scales accessible on experimental time scales so that the mechanism behind the rejuvenation found in experiments is of a different origin.[5,25,26,42,43] In order to shed light on these intriguing issues we study in detail the crossover from weakly to strongly perturbed regimes of the chaos effects following recent studies.[21,30,35]

The other major theoretical basis is the ghost domain scenario,[20,22] which suggests dynamical memory effects that survive under strong rejuvenation due to the chaos effect. This scenario explicitly takes into account the remanence of a sort of symmetry-breaking field or *bias* left in the spin configuration of the system by which "memory" is imprinted and retrieved dynamically. We carefully investigate the memory-retrieval process, called *healing* of the original domain structure,[22] which takes a macroscopic time. In previous studies, the importance of this process has not received enough attention. A traditional interpretation of the memory phenomena was based on *hierarchical phase space pictures*.[44] In the ghost domain scenario there is no need for such built-in, static phase space structures. Some predictions of the ghost domain scenario are also markedly different from conventional *real space* pictures including earlier phenomenological theory, such as that of Koper and Hilhorst[45] and others,[26,42] which do not account for the role of the remanent bias.

It should be remarked that some basic assumptions of the droplet picture are debated and alternative pictures have been proposed, which include proposals of anomalously low-energy excitations with an apparent stiffness exponent $\theta=0$.[46–48] However, in the present paper we concentrate on working out detailed comparisons between the theoretical outcomes of the original droplet theory and experimental and numerical results.

A. Edwards-Anderson model

In this section we consider a $\pm J$ Edwards-Anderson Ising spin-glass model defined by the Hamiltonian,

$$H = -\sum_{\langle ij \rangle} J_{ij} S_i S_j - h \sum_i S_i. \tag{1}$$

The Ising spin S_i is put on a lattice site $i (i=1,\ldots,N)$ on a d-dimensional (hyper-)cubic lattice. The interactions J_{ij} are quenched random variables drawn with equal probability among $\pm J$ with $J>0$, and h is an external field. In the following we choose the Boltzmann's constant to be $k_B=1$ for simplicity.

The original form of the droplet theory only concerns Ising spin glasses, but we assume that essentially the same picture also applies for vector spin glasses. Recently it has been found from a Migdal-Kadanoff renormalization group analysis, e.g., that vector spin glasses exhibit qualitatively similar but quantitatively much stronger chaos effects than Ising spin glasses.[49]

B. Overlaps between equilibrium states of different environments

We assume that an equilibrium spin-glass state $\Gamma^{(T,\mathcal{J})}$ is represented by its *typical* spin configuration specified as $\sqrt{q_{\rm EA}}(T)\sigma_i^{(T,\mathcal{J})}$ where $i=1\ldots N$. Here T is a temperature below the spin-glass transition temperature T_g and $\mathcal{J}$ represents a given set of bonds J_{ij}. The parameter $q_{\rm EA}(T)$ is the Edwards-Anderson order parameter, which is 1 as $T\to 0$ and decreases by increasing T due to thermal fluctuations. Apart from the thermal fluctuations parametrized by $q_{\rm EA}$, the typical spin configuration is represented by the *backbone* spin configuration represented by quenched-random variables $\{\sigma_i^{(T,\mathcal{J})}\}$, which takes Ising values ± 1. Furthermore, we assume that the only other possible equilibrium state at the same environment $(T,\mathcal{J})$ is $\overline{\Gamma^{(T,\mathcal{J})}}$ whose configuration is given by $-\sqrt{q_{\rm EA}}(T)\sigma_i^{(T,\mathcal{J})}$.

The scaling theory[16–18] suggests the chaos effect: the backbone spin configuration $\{\sigma_i^{(T,\mathcal{J})}\}$ changes significantly by slight changes in the environment $(T,\mathcal{J})$. Our interest in the present paper is to investigate how this effect is reflected on the dynamics. Let us consider two sets of different environments $A=(T,\mathcal{J})$ and $B=(T',\mathcal{J}')$, which are specified from the following:

(i) Temperature change. The temperature-change simply means $T'=T+\Delta T$ with an *infinitesimal* ΔT and $\mathcal{J}=\mathcal{J}'$.

(ii) Bond change. The set of bonds $\mathcal{J}'$ is created from $\mathcal{J}$ by changing the *sign* of an *infinitesimal* fraction p of $\mathcal{J}$ randomly while $T=T'$. As noted in Ref. 37 this amounts to a perturbation of strength $\Delta J \sim J\sqrt{p}$.

The relative differences between the backbone spin configurations may be detected by introducing the *local overlap*

$$O_i^{AB} = \sigma_i^A \sigma_i^B, \tag{2}$$

which takes Ising ± 1 values. In Fig. 1, a schematic picture of the configuration of the local overlap $\{O_i^{AB}\}$ is shown. The

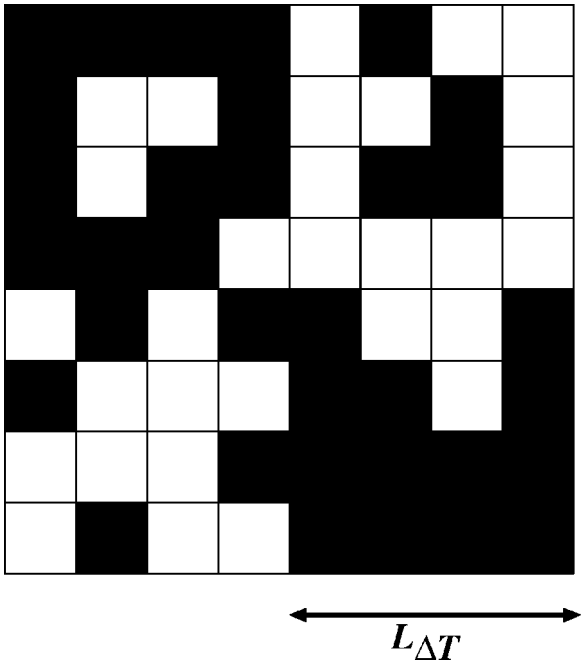

FIG. 1. A schematic picture of the configuration of the local overlap O_i^{AB} between the equilibrium state Γ_A and Γ_B. The black and white represents ±1 values of the local overlap. As a first approximation, the configuration of the local overlap can be described as a collection of "blocks" of linear size of the overlap length $L_{\Delta T}$ within which the sign of the overlap is biased to positive (black) or negative (white). However, there are minorities within the blocks that have the opposite sign of those of the majorities.

spatial pattern of the local overlap can be decomposed into *blocks*. The value of the local overlap O^{AB} is essentially *uniform* (either +1 or −1) within a given block while the values on different blocks are completely uncorrelated. The correlation length of the local overlaps, which is the typical size of the blocks, corresponds to what is called the *overlap length*[16,17] between Γ_A and Γ_B. In the case of temperature changes, the overlap length is given by

$$L_{\Delta T} = L_0 \left(\frac{s(T)|\Delta T|}{\Upsilon(T)} \right)^{-1/\zeta}, \tag{3}$$

where L_0, $\Upsilon(T)$, and $\zeta(>0)$ are the unit length scale, the stiffness constant, and the chaos exponent, respectively. The factor $s(T)$ describes the temperature dependence of the droplet entropy.[33] For the case of bond perturbations, the overlap length associated with a bond perturbation of strength ΔJ is expected to scale as

$$L_{\Delta J} = L_0 (|\Delta J|/J)^{-1/\zeta} \tag{4}$$

with[37] $|\Delta J| \sim J\sqrt{p}$. Note that the chaos exponent ζ is expected to be the same for both temperature and bond chaos. We emphasize that a strong bond-chaos effect induced by an *infinitesimal* change of the bonds is as nontrivial as the temperature chaos effect. It should be noted that such a sensitive response to a perturbation does not happen in nonfrustrated systems, such as simple ferromagnets.

The above picture is the simplest one, which only takes into account *typical* aspects of the chaos effect. Let us present an improved discussion on how the bulk of the equilibrium spin-glass state is affected by perturbations on various length scales. It will lead us to find a crossover from a *weakly perturbed regime* $L \ll L_{\Delta T}$ to a *strongly perturbed regime* $L \gg L_{\Delta T}$. For simplicity, let us decompose a block of size $L_{\Delta T}^d$ into smaller subblocks of linear size $L_n = L_{\Delta T}/2^n$ with $n = 1, 2, \ldots$. The *majority* of the subblocks will have a common value of the local overlap O^{AB} (either +1 or −1). However, there will be *minority* subblocks, which have the opposite sign of the overlap with respect to the majority. The probability $p_{\rm minor}$ that a subblock belongs to such a minority group is expected to be a function of the scaled length $y = L_n/L_{\Delta T} = 2^{-n}$. In the weakly perturbed regime $y \ll 1$, the probability scales as[21,35]

$$p_{\rm minor}(y) \propto y^{\zeta}, \quad y \ll 1. \tag{5}$$

Note that $p_{\rm minor}$ is simply proportional to $|\Delta T|$ or $|\Delta J|$ as can be seen by inserting Eq. (3) or (4) into Eq. (5). The presence of the minority phase is due to marginal droplets with vanishingly small free-energy gap, which easily responds to perturbations.[21,30,35] For a detailed discussion see Refs. 21 and 35. Note that the probability $p_{\rm minor}(y)$ increases with increasing length (y) and saturates to 1 as $y \to 1$.

C. Relaxation in a fixed working environment

Consider aging in a given working environment $A = (T_A, \mathcal{J}_A)$ after a rapid temperature quench from above the spin-glass transition temperature T_g down to a working temperature T_A below T_g. We suppose that aging can be understood in terms of *domain growth*. Let us start by giving a general definition of a *domain*. First, we average out short-time thermal fluctuations on the temporal spin configuration $S_i(t)$. Then the spin configuration at time t may be represented by $\sqrt{q_{\rm EA}(T_A)}s_i(t)$. Here $s_i(t)$ is an Ising variable that represents a coarse-grained temporal spin configuration. Second, we project this spatiotemporal spin configuration onto any desired reference equilibrium state Γ_R at an environment $R = (T_R, \mathcal{J}_R)$,

$$\tilde{s}_i^R(t) = \sigma_i^R s_i(t). \tag{6}$$

Now we define a *domain* with respect to the general reference state Γ_R. It has the following two essential properties:

- A domain belonging to Γ_R (or $\overline{\Gamma_R}$) is a local region in the space within which the *sign* of the projection $\tilde{s}_i^R$ is *biased* to either positive or negative. The spatial variation of the sign of the bias defines the geometrical organization of domains, i.e., domain wall configuration.
- The *amplitude of the bias* in the interior of a domain is the *order parameter* defined as

$$\rho_R(t) = \left| \frac{1}{\mathcal{N}_R} \sum_{i \in \text{a domain of } \Gamma_R} \tilde{s}_i^R(t) \right|, \tag{7}$$

where $\mathcal{N}_R$ is the number of spins belonging to the domain. The amplitude of the bias can be smaller than 1, indicating that the interior of the domain is "ghostlike" (see Fig. 2).

To avoid confusion, let us note that the order parameter de-

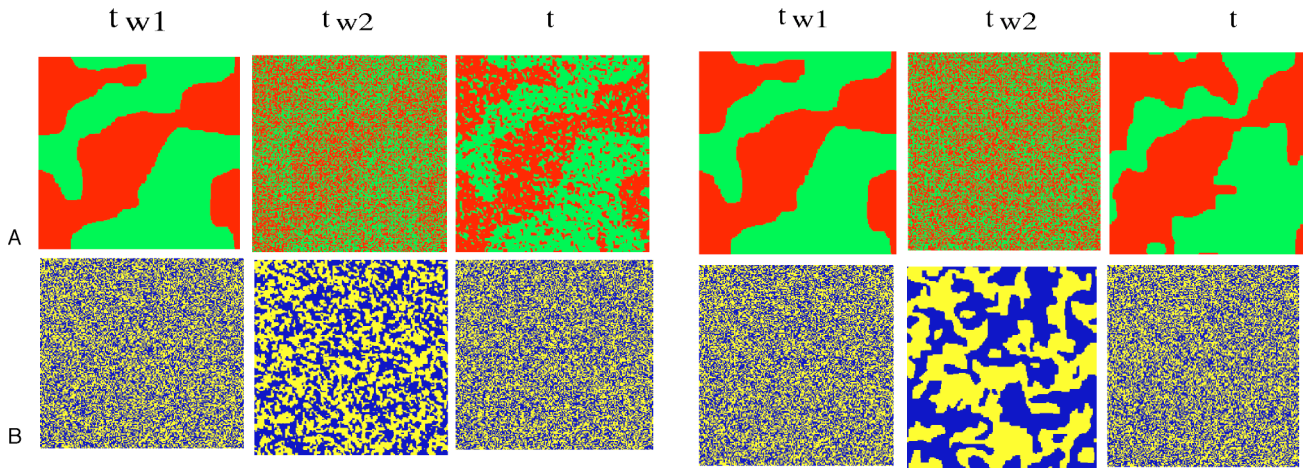

FIG. 2. (Color online) An illustration of the evolution of ghost domains in a "perturbation-healing" protocol at large length scales. The above pictures are generated by an artificial simulation: Monte Carlo simulation is performed on a set of Ising spins on a square lattice by cycling the working Hamiltonian given by Mattis models whose ground states are exactly given by σ^A and σ^B (see Ref. 51 for the details). The different colors represent the sign + and − of the projections $\tilde{s}_i^A(t)$ (top figures) and $\tilde{s}_i^B(t)$ (bottom figures) at the end of initial aging state of duration t_w, at the end of the perturbation stage of duration τ_p and after time τ_h in the healing stage. Here the backbone spin configuration of the target equilibrium states σ^A and σ^B are completely unrelated random configurations so that the local overlap $O_i^{AB}=\tilde{s}_i^A(t)\tilde{s}_i^B(t)=\sigma^A\sigma^B$ [see Eq. (8)] is a completely random configuration: the overlap length is just 1 in the unit lattice. The remanent bias at the end of the perturbation stage is found as (left) $\rho_{\rm rem}\sim 0.15$ and (right) $\rho_{\rm rem}\sim 0.04$. In the former the human eyes just barely distinguish the ghost domains, whereas in the latter the domains have become indistinguishable. In both cases, the strength of the bias increases up to $O(1)$ in the healing stage: (left) $\rho_{\rm rec}\sim 0.59$ and (right) $\rho_{\rm rec}\sim 0.58$.

fined above is different from the EA-order parameter $q_{\rm EA}$, which parametrizes the thermal fluctuations on top of the backbone spin configuration.

The natural choice for the reference equilibrium state is $R=A$, i.e., the equilibrium state Γ_A, of the working environment $A=(T_A,\mathcal{J}_A)$ itself. After time t from the temperature quench, domains belonging to Γ_A and $\overline{\Gamma}_A$ will have a certain typical size $L_{T_A}(t)$. The domain size $L_{T_A}(t)$ will grow very slowly by activated dynamics. Here the subscript T_A is used to emphasize the temperature dependence of the growth law [see Eq. (A2)]. (The growth law is discussed in detail in Appendix A.) Note in this context that the order parameter ρ_A [Eq. (7)] within the domains belonging to Γ_A and $\overline{\Gamma}_A$ takes the maximum value 1 constantly during isothermal aging.

Let us now consider more generally what is happening on the reference states associated with different environments during isothermal aging, i.e., $R\neq A$. As illustrated schematically in Fig. 3, the domains of the reference states at different environments $R\neq A$ will grow with time up to the overlap length between Γ^A and Γ^R. Concerning this point it is useful to note the relation between the projections $\tilde{s}_i^R(t)$ and $\tilde{s}_i^A(t)$ given by

$$\tilde{s}_i^R(t)=O_i^{AR}\tilde{s}_i^A(t), \tag{8}$$

which immediately follows from Eq. (6). Here O_i^{AR} is the overlap between the equilibrium state Γ_A and Γ_R defined in Eq. (2). The spatial pattern of overlap O_i^{AR} is roughly uniform over the length scale of the overlap length $L_{\Delta T}$ between Γ_A and Γ_R. Beyond $L_{\Delta T}$, however, the configuration of the overlap O_i^{AR} is random. Then it follows that the growth of domains belonging to Γ_A (and $\overline{\Gamma}_A$) only contributes to the growth of domains belonging to Γ_R (and $\overline{\Gamma}_R$) up to the overlap length. Thus we expect that at environment R the typical domain size, which we denote as effective domain size $L_{\rm eff}(t)$, should scale as[28,30]

$$L_{\rm eff}(t)=L_{\Delta T}F\left(\frac{L_{T_A}(t)}{L_{\Delta T}}\right). \tag{9}$$

The scaling function $F(x)$ reflects the following three regimes as the age of the system t_w increases:

(i) *Accumulative regime*. At length scales much shorter than the overlap length $L_{\Delta T}$, the growth of the domains be-

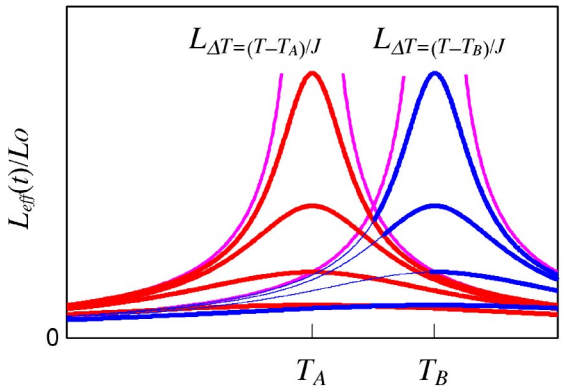

FIG. 3. (Color online) A schematic illustration of the temperature profiles of the effective domain size around the working temperatures T_A and T_B. The solid and dotted lines represent the effective domain size $L_{\rm eff}(t)$ at logarithmically separated times t during isothermal aging at T_A and T_B, respectively.

longing to Γ_A leads to the growth of the domains belonging to Γ_R such that $L_{\rm eff}(t_w)=L_{T_A}(t_w)$. This yields

$$\lim_{x\to 0} F(x) = x. \tag{10}$$

(ii) *Weakly perturbed regime*. As we discussed in the previous subsection, the chaos effect emerges gradually at length scales shorter than the overlap length. We now want to determine the first correction term to Eq. (10) due to defects at the scale of $L_{T_A}(t)$. Intuitively, we assume that $L_{\rm eff}$ is analytic and an even function of ΔT (and ΔJ). We also expect that the correction term is an analytic function of $p_{\rm minor}$ [see Eq. (5)], which is proportional to $|\Delta T|$ (and $|\Delta J|$). Combining these we find that the first correction term should be $O(p_{\rm minor}^2)$ leading to[50]

$$F(x) = x(1 - cx^{2\zeta}), \quad x \ll 1. \tag{11}$$

We note that because of defects at length scales $L \ll L_{T_A}(t)$, the order parameter ρ_R [Eq. (7)] is smaller than $\rho_A=1$.

(iii) *Strongly perturbed regime*. The domains belonging to Γ_R can, by aging at A, only grow to the size of the upper bound $L_{\Delta T}$, yielding $L_{\rm eff}(t_w)=L_{\Delta T}$. This requires

$$F(x) = 1, \quad x \gg 1. \tag{12}$$

D. Relaxation after shift of working environments

Let us now consider a shift of working environment $A \to B$ after aging the system in the environment A for a time t_w. Γ_B is the reference state because the working environment is now B. Just after the T shift, the sizes of the domains Γ_B associated with the environment B (at temperature T_B) is given by the effective domain size $L_{\rm eff}(t_w)$ in Eq. (9) (see Fig. 3). Thus the spin configuration just after the temperature shift $T_A \to T_B$ is equivalent to that after usual isothermal aging done at B for a certain waiting time $t_{\rm eff}$ (after direct temperature quench from above T_g down to T_B). The *effective time*, $t_{\rm eff}$, is defined through

$$L_{T_B}(t_{\rm eff}) = L_{\rm eff}(t_w). \tag{13}$$

Since $L_{\rm eff}(t_w)$ is limited by the overlap length $L_{\Delta T}$, *rejuvenation* occurs after the temperature (or bond) shifts: the system looks *younger* [i.e., $L_{T_B}(t_{\rm eff}) < L_{T_A}(t_w)$] than it would have been if the aging was fully accumulative [i.e., $L_{T_B}(t_{\rm eff}) = L_{T_A}(t_w)$].

The effective time $t_{\rm eff}$ can be determined experimentally by measuring the ZFC relaxation after temperature and bond shifts (see Sec. IV). As in the isothermal case,[6] a crossover occurs between quasiequilibrium and out-of-equilibrium dynamics at $L_{T_B}(t) \sim L_{T_B}(t_{\rm eff})$, where $L_{T_B}(t)$ is the length scale on which the system is observed at time t after the temperature (or bond) shift.

Now let us turn our attention to what happens to the amplitude of order parameters within the domains after T shifts.

• The order parameter ρ_B within domains belonging to Γ_B evolves as follows. Although the system is essentially equilibrated with respect to B up to the effective domain size $L_{\rm eff}(t_w)$, it contains some defects that cause a certain reduction of the order parameter. These defects are progressively eliminated after the T shift and ρ_B approaches the full amplitude 1. At time t after the shift of environment, such defects smaller than $L_{T_B}(t)$ are eliminated, but the larger ones still remain. Thus, this process finishes once defects as large as the domain size $L_{\rm eff}$ are removed. The time scale needed to finish this transient process is given by

$$L_{T_B}(t_{\rm trans}) = L_{\rm eff} \tag{14}$$

thus $t_{\rm trans} \sim t_{\rm eff}$ because of Eq. (13).

• The order parameter within domains belonging to equilibrium states at other temperatures $T \neq T_B$ evolves as follows. At length scales greater than $L_{\Delta T=(T-T_B)/T}$ (see Fig. 3) the domains grown before the T shift suffer a progressive reduction of the order parameter. However, the spatial pattern of the *sign of the bias* remains the same as before the T shift (see Fig. 2). This is a very important point that we discuss in detail in Sec. II E.

Let us also remark that the population of thermally active droplets at a certain scale L, which is proportional to[17] $(k_BT/J)(L/L_0)^{-\theta}$, cannot follow sudden changes of the working temperatures, but needs a certain time to be switched off (or switched on). Progressive adjustments of the population of thermally active droplets take place on the time scale $t_{\rm trans}$ defined in Eq. (14).

In experiments, the progressive elimination of the remanent defects on domains belonging to Γ_B after the shifts should give rise to certain excessive contributions to the relaxation of the magnetic susceptibility with the duration time $t_{\rm trans}$ given above. The amplitude of the excessive response is expected to be proportional to ΔT or ΔJ. This is because both the population of the isolated defects due to the chaos effect in the weakly perturbed regime [see Eq. (5)] and the excessive thermal droplets are proportional to ΔT or ΔJ.

E. Relaxation under cyclings of working environments

We are now in position to discuss dynamics under cycling of working environments, such as temperature cycling. Here we consider the simplest protocol. (i) *Initial aging stage*: after a temperature quench from above T_g, the system is aged for a time t_{w_1} within environment $A-(T_A, \mathcal{J}_A)$. (ii) *Perturbation stage*: a "perturbation" is then applied, and the system is aged for a time t_{w_2} at the new environment $B-(T_B, \mathcal{J}_B)$. (iii) *Healing stage:* Finally, the working environment is brought back to A where the spin structure obtained in the initial aging stage slowly "heals" from the effects of the perturbation.

1. Weakly perturbed regime

Let us focus on what is happening on length scales shorter than the overlap length $L_{\Delta T}$ during the one-step cycling introduced above. This will be relevant for observations at correspondingly short time scales in experiments and simulations. The effect of the change of working environments should be *perturbative* in the weakly perturbed regime $L < L_{\Delta T}$ as we discuss below.

During the perturbation stage, the growth of domains belonging to Γ_B introduces rare defects of size L on top of the

domains belonging to Γ_A with a probability proportional to $(L/L_{\Delta T})^{\zeta} \ll 1$ [see Eq. (5)]. Because the probability is low, these defects are isolated from each other. During the healing stage, these islandlike objects are progressively removed one by one from the small ones up to larger ones. Since the maximum size of such a defect is $L_B(t_{w_2})$, we find that the removal of the defects will be completed in a time scale $t_{\rm rec}^{\rm weak}$ given by

$$L_A(t_{\rm rec}^{\rm weak}) = L_B(t_{w_2}). \tag{15}$$

Here the superscript "weak" indicates that the formula is valid only in the weakly perturbed regime. After this recovery time, the original state of the interior of the domains belonging to Γ_B is restored. Finally, let us also note that domain size at A continues to grow during the aging at B and vice-versa within the weakly perturbed regime.

2. Strongly perturbed regime

Suppose that the length scales explored during the three stages $L_{T_A}(t_{w_1})$, $L_{T_B}(t_{w_2})$, and $L_{T_A}(t)$ are all greater than the overlap lengths $L_{\Delta T}$. Then, the strongly perturbed regime of the chaos effect (see Sec. II B), which appears at length scales greater than the overlap length $L_{\Delta T}$, should come into play. Figure 2 gives an illustration of how projections $\tilde{s}_i^A(t)$ and $\tilde{s}_i^B(t)$ evolves at length scales greater than the overlap length. The unit of length scale is chosen to be the overlap length $L_{\Delta T}$. Thus the pattern of the local overlaps O_i^{AB} is completely random beyond the unit length scale.

In the initial aging stage, the domains belonging to Γ^A grow up to the size $L_{T_A}(t_{w_1})$. The amplitude of the order parameter within the domains has the full amplitude (1) everywhere.

In the perturbation stage, the system is relaxing in the environment B. Since the spin configuration before the perturbation stage is completely random with respect to B beyond the overlap length $L_{\Delta T}$, the domains belonging to Γ^B grow independently of the previous aging. In the meantime, the domains belonging to Γ^A become ghostlike, i.e., they keep their overall "shape" while their interior becomes *noisy* due to the growth of domains belonging to the reference state B. The remanent strength of the order parameter of A defined in Eq. (7),

$$\rho_{\rm rem}(t) = \left| \frac{1}{\mathcal{N}^A} \sum_{i \in \text{a domain of } \Gamma_A} \tilde{s}_i^A(t) \right|, \tag{16}$$

slowly decays with time t. Here $\mathcal{N}_A \sim [L_{T_A}(t_w)/L_0]^d$ is the number of spins belonging to a domain of Γ_A. After time t from the beginning of the perturbation stage it becomes,[20,22]

$$\rho_{\rm rem}(t) \sim \left[\frac{L_{T_B}(t)}{L_{\Delta T}} \right]^{-\bar{\lambda}} \tag{17}$$

where $\bar{\lambda}$ is a dynamical exponent. The crucially important point is that the spatial pattern of the *sign* of the local bias (order parameter)—with decreasing amplitude of strength $\rho_{\rm rem}(t)$—is preserved during the perturbation stages. We call this spatial structure a *ghost domain*. Such ghost domains are responsible for the memory effect allowed after full rejuvenation induced by the chaos effect.

In the healing stage, the domains belonging to Γ_A start to grow from the unit length scale $L_{\Delta T}$ all over again. However, the initial condition for this healing stage is *not* completely random, since ghost domains with bias $\rho_{\rm rem}(t_{w_2})$ exist. We thus need to consider domain growth with a slightly biased initial condition.[52] The bias now *increases* with time as[22]

$$\rho_{\rm rec}(t;\rho_{\rm rem}) \sim \rho_{\rm rem}(t_{w_2}) \left(\frac{L_{T_A}(t)}{L_{\Delta T}} \right)^{\lambda}. \tag{18}$$

Since the size of the ghost domain itself is finite, it also continues to grow during the healing stage. Following Ref. 20 we call the growth of the bias inside a ghost domain during the healing stage *inner coarsening* and the further growth of the size of the ghost domain itself *outer coarsening*.

The growth of the bias stops when the bias (order parameter) saturates to the full amplitude. This defines the *recovery time* $t_{\rm rec}^{\rm strong}$,

$$\rho_{\rm rec}(t_{\rm rec}^{\rm strong};\rho_{\rm rem}) \sim 1 \quad L(t_{\rm rec}^{\rm strong})/L_{\Delta T} \sim \rho_{\rm rem}^{-1/\lambda}. \tag{19}$$

Combining this with Eq. (17), the relation[22]

$$\frac{L_{T_A}(t_{\rm rec}^{\rm strong})}{L_{\Delta T}} = \left(\frac{L_{T_B}(t_{w_2})}{L_{\Delta T}} \right)^{\bar{\lambda}/\lambda} \tag{20}$$

is obtained. Here, the superscript "strong" indicates that the formula is valid only in the strongly perturbed regime.

An important remark is that the two exponents λ and $\bar{\lambda}$ are generally different. In Ref. 52, a scaling relation $\bar{\lambda}+\lambda = d$ was found. Only in the special case $\lambda = \bar{\lambda}$, which happens, e.g., in the spherical model considered in Ref. 20, the relation Eq. (20) is accidentally simplified to $L_{T_A}(\tau_{rec}^{\rm strong}) = L_{T_B}(\tau_p)$. Concerning the exponent $\bar{\lambda}$, the inequality is proposed as[18] $d/2 \leqslant \bar{\lambda} < d$. Combining that with $\bar{\lambda}+\lambda = d$, a useful inequality is obtained,[22]

$$\bar{\lambda}/\lambda \geqslant 1. \tag{21}$$

In Ref. 22, the 4D Ising EA model was studied and it was found that $\bar{\lambda} \sim 3.2$ and $\lambda \sim 0.8$. In this case and also for 3D systems in general, the recovery time is very large $t_{\rm rec}^{\rm strong} \gg t_{\rm rec}^{\rm weak}$.

The above results are markedly different from what one would expect from conventional "real-space" or "phase-space" arguments, which neglect the role of bias. If such a mechanism causing a symmetry breaking is absent, the "new domains" grown during the healing could often have the wrong sign of bias with respect to the original one leading to total erasure of memory. In contrast to the hierarchical phase-space models,[44] the ghost domain scenario predicts memory also in the positive T-cycling ($T_A < T_B$) case. Indeed such examples are already reported (see Fig. 6 in Ref. 44 and Fig. 3 in Ref. 53).

3. Multiplicative rejuvenation effect

The above considerations for one-step cycling can be extended to multistep cycling cases. At large length scales beyond the overlap length, some quite counterintuitive predictions follow due to the multiplicative nature of the noise effect.[20] For example, in a T-cycling $T_A(t_{w_1}) \rightarrow T_B(t_{w_2}) \rightarrow T_C(t_{w_3}) \rightarrow T_A$, the amplitude of the order parameter of A is reduced to $\rho_{\rm rem} \sim \rho_B \times \rho_C$ in the end of the second perturbation. Here ρ_B and ρ_C represent reductions due to domain growth at B and C. Thus, the recovery time $t_{\rm rec}^{\rm strong}$ of the order parameter of A becomes

$$\frac{L_{T_A}(t_{\rm rec}^{\rm strong})}{L_{\Delta T}} = \left[\frac{L_{T_B}(t_{w_2})}{L_{\Delta T}} \frac{L_{T_C}(t_{w_3})}{L_{\Delta T}} \right]^{\bar{\lambda}/\lambda}. \qquad (22)$$

This tells that sequential short time perturbations can cause huge recovery times. Let us note that this multiplicative rejuvenation effect is absent at length scales smaller than the overlap length $L_{\Delta T}$. At such short length scales, changes of temperature (or bonds) only amount to put isolated islandlike defects on the domains, which rarely overlap with each other. The multiplicative effect discussed above is hardly expected within conventional pictures, which do not contain the time evolution of the bias (order parameter).

F. Freezing of aging by slow changes of working environments: Heating and cooling rate effects

The effect of finite heating and cooling rates is a very important problem from an experimental point of view. Even the fastest cooling and heating rates, such as those used in "temperature quench" experiments, are always extremely slow compared to the atomic spin flip time $\tau_m \sim \hbar/J \sim 10^{-13}$ s. Typically, the maximum experimental heating or cooling rate is $v_T \sim O(10^{-1})$ K/s and $T_g \sim O(10)$ K (see Appendix B), which in simulations would be equivalent to an extremely slow heating or cooling rate of $v_T \sim 10^{-15} T_g$/MCS (Monte Carlo steps). Thus, the instantaneous changes in the working environments assumed in the previous sections are very unrealistic, at least experimentally.

Nonetheless, we expect that the effect of a finite heating and/or cooling rate can be taken into account by introducing a characteristic length scale $L_{\rm min}(v_T, T)$. As discussed in Ref. 22, it is natural to expect that the competition between accumulative and chaotic (rejuvenation) processes during a slow change in working environments, either temperature or bond changes, results in a sort of freezing of aging, such that the effective domain size with respect to the temporal working environment becomes a constant in time $L_{\rm min}(v_T, T)$. This domain size is expected to decrease when the rate of the changes increases, e.g., the heating or cooling rate v_T. The characteristic length $L_{\rm min}(v_T, T)$ can be seen as a *renormalized overlap length* in the following senses:

- The frozen age $t_{\rm min}$ given by $L_T(t_{\rm min}) = L_{\rm min}(v_T, T)$ sets the minimum time scale for the start of the domain growth when the target temperature T is just reached after continuous temperature changes. This effect can be readily seen experimentally as we discuss in Secs. IV A and B 2.
- The overlap length $L_{\Delta T}$ appearing in Eqs. (20) and (22) should be replaced by $L_{\rm min}(v_T, T)$. The latter should be greater than the overlap length $L_{\Delta T}$ between the equilibrium states at two temperatures connected by a continuous temperature change. Thus, the finiteness of the heating and/or cooling rate can significantly reduce the recovery times for the memories.

Indeed, it is known from previous experimental studies that cooling and heating rate effects are nonaccumulative and that it is only the rate very close to the target temperature that affects the observed isothermal aging behavior.[7,8] However, within this narrow temperature region around the target temperature, heating and cooling rate effects were found to be relevant, but as long as the employed observation time is made long, even a cooling rate with $v_T \sim O(10^{-1})$ K/s can be regarded as a "quench" that allows experimental observations of nonequilibrium dynamical scaling properties of isothermal aging starting from a random spin configuration.[29,44] An interpretation of this feature would be that the observation times used in the experiments are actually larger than the effective age $t_{\rm min}$ related to the renormalized overlap length. This remarkable feature is quite different from that of other glassy systems governed by simple thermal slowing down, such as supercooled liquids,[54] in which the effect of aging at different temperatures during the heating and/or cooling only add up accumulatively. It may be argued that the unusual cooling rate *independence* of the dynamics in spin glasses already in itself supports the relevance of the temperature-chaos concept.

G. Comparisons to the classical Kovacs effect

The mechanisms and nature of the memory effects involving length scales shorter and longer than the overlap length are markedly different within the ghost domain scenario. After a change of working environments involving only short length scales, the chaos effect is weak (perturbative) and the system is not rejuvenated. Such nonchaotic *perturbative* effects yield, as discussed in Sec. II E 1, the trivial recovery time given by Eq. (15). This recovery time fits well with conventional intuition based on "length scales" or "phase space." Such effects may be understood as classical memory effects in a *fixed-energy landscape*[5] known as Kovacs effects in polymer glasses,[27] which do not accompany a real rejuvenation. It is reasonable to expect that Kovacs effects exist in a broad class of systems[5,26,55,56] as far as the chaos effects are absent or irrelevant. The fixed-energy landscape picture is valid only at length scales shorter than the overlap length, where defects are approximately independent of each other. For perturbations involving length scales greater than $L_{\Delta T}$, this picture becomes totally invalid and the scenario outlined above for the strongly perturbed regime is required.

III. INTRODUCTION TO EXPERIMENTS AND SIMULATIONS

A. Experiments

The nonequilibrium dynamics of two canonical spin glasses was investigated using superconducting quantum interference device (SQUID) magnetometry. The samples are a

single crystal of $Fe_{0.5}Mn_{0.5}TiO_3$ ($T_g \approx 21.3$ K), the standard Ising spin-glass,[57,58] and a polycrystalline sample of the Heisenberg Ag(11 at% Mn) spin glass ($T_g \approx 32.8$ K). The experiments were performed in noncommercial SQUID magnetometers,[59] designed for low-field measurements and optimum temperature control (see Appendix B for details).

Experimental results for the two samples will be presented using the following thermal procedures:

(i) In an isothermal aging experiment, the sample is quenched (cooled as rapidly as possible) from a temperature above the transition temperature to the measurement temperature T_m in the spin-glass phase. In dc measurements, the relaxation of the ZFC magnetization is recorded in a small probing field after aging the sample in zero field for a time t_w at the measurement temperature.

(ii) In a T-shift experiment (Sec. IV A) the sample is, after a quench, first aged at T_i before measuring the relaxation at $T_m = T_i + \Delta T$.

(iii) In a T-cycling experiment (Sec. V A) the sample is first aged at T_m, then at $T_m + \Delta T$ and, subsequently, the relaxation is recorded at T_m.

(iv) In a temperature memory experiment[7,60] (Sec. VI) the system is cooled from a temperature above the transition temperature to the lowest temperature. The cooling is interrupted at one or several temperatures in the spin-glass phase. The magnetization is subsequently recorded on reheating.

In experiments (i)–(iii), all temperature changes are made with the maximum cooling rate ($v_{\text{cool}} \sim 0.05$ K/s) or maximum heating rate ($v_{\text{heat}} \sim 0.5$ K/s). A temperature quench, therefore, refers to a cooling with the maximum cooling rate. The magnetic fields employed in the experiments are small enough ($h \approx 0.1-1$ Oe) to ensure a linear response[60] of the system.

To shortly illustrate the rejuvenation and memory phenomena, which are examined in detail in this article, we show in Fig. 4 a negative T-cycling experiment on the Ag(11 at% Mn) sample. The ac susceptibility is measured as function of time after a temperature quench. The system is aged at 30 K for 3000 s, afterward the temperature is changed to 28 K for 3000 s, and finally, it is changed back to 30 K. The isothermal aging at 30 K and 28 K are shown as references. We first notice that the aging at 28 K is the same in the cycling experiment as after a direct quench. Hence, at 28 K, the system appears unaffected by the previous aging at 30 K—the system is *completely rejuvenated* at the lower temperature. However, some time (t_{rec}) after changing the temperature back to 30 K, the ac signal is the same as if the aging at 28 K had not taken place; despite the rejuvenation at 28 K the system keeps a *memory* of the aging at 30 K. One of our major interests is to clarify if the memory recovery process with duration t_{rec} can be understood in terms of the ghost domain picture (Sec. II).

B. Simulations

Standard heat-bath Monte Carlo simulations of the EA Ising model (introduced in Sec. II A) on the four-dimensional hypercubic lattice ($T_g = 2.0J$)[61] were performed following protocols (i)–(iii), but using a bond change $\mathcal{J}_A \rightarrow \mathcal{J}_B$ instead of a temperature change. The initial conditions are random spin configurations to mimic a direct-temperature quench (with $v_T = \infty$) to $T < T_g$. Detailed comparisons of the effects of bond perturbations and temperature changes allows us to clarify the common mechanism of rejuvenation and memory effects. An important advantage of the numerical approach is that the dynamical length scale $L_T(t)$ can be obtained directly in the simulations.[62,63] Details of the model and the simulation methods are given in Appendix C.

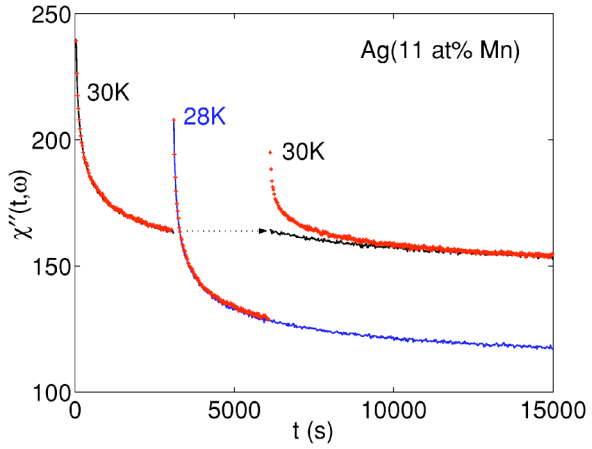

FIG. 4. (Color online) The ac susceptibility versus time after a temperature quench. A temperature cycling from 30 K to 28 K and back to 30 K is shown as pluses. The solid lines are the isothermal aging at 28 K and 30 K. After the negative T shift from 30 K to 28 K, the system is *completely rejuvenated*. Still, after the T cycling it keeps a *memory* of the first aging at 30 K. $f = 510$ mHz.

IV. REJUVENATION EFFECTS AFTER TEMPERATURE AND BOND SHIFTS

In this section, we present a quantitative study of the rejuvenation effect using T-shift experiments and bond-shift simulations.

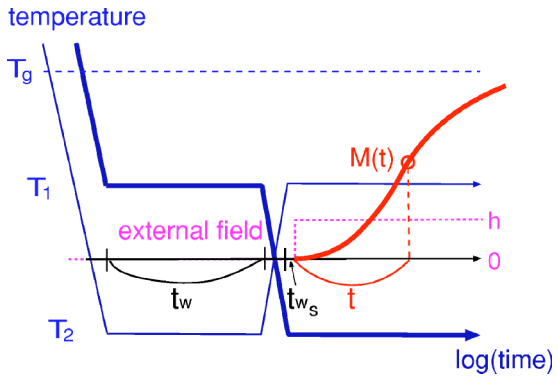

FIG. 5. (Color online) Schematic representation of a *twin* T-shift experiment. In the experiment represented using the thick line $(T_i, T_m) = (T_1, T_2)$, while $(T_i, T_m) = (T_2, T_1)$ in the experiment represented by the thin line. In ac experiments, $\chi(t)$ is also monitored during the halt at T_i. In order to ensure thermal stability at T_m, a short waiting time $t_{ws} = 3$ s is needed before applying the magnetic field and recording the ZFC relaxation (Ref. 64).

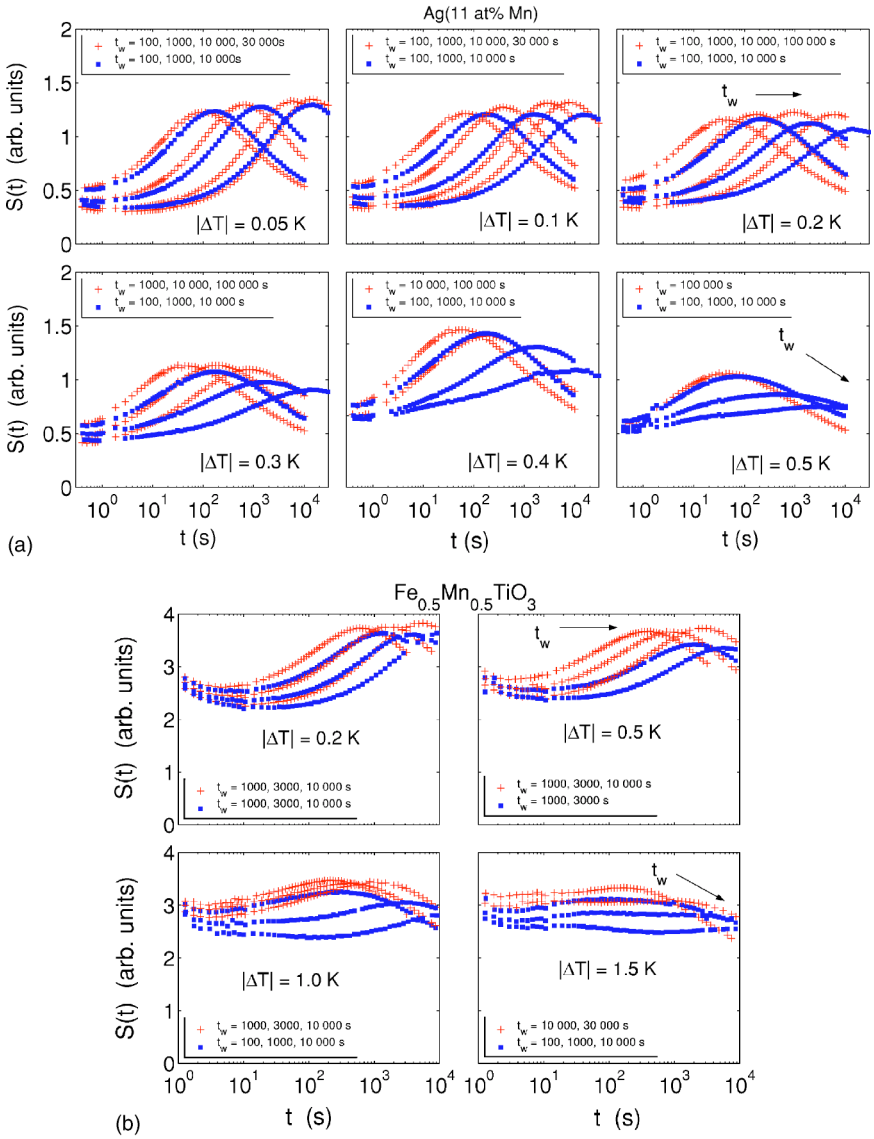

FIG. 6. (Color online) Relaxation rate versus time after positive and negative twin T-shift measurements. Pluses are positive T shifts (T_1, T_2), while squares are negative T shifts (T_2, T_1). (a) Ag(11 at% Mn): $T_1 = 30 - |\Delta T|$ K and $T_2 = 30$ K. (b) $Fe_{0.5}Mn_{0.5}TiO_3$: $T_1 = 19 - |\Delta T|$ K and $T_2 = 19$ K. Note that for each Δt the peak position t_{max} increases with t_w and the maximum in $S(t)$ broadens, which suggests that these data reflect the weakly perturbed regime of the temperature-chaos effect. (See Fig. 11 for the corresponding data of bond shifts in the 4D EA model.)

A. Temperature-shift experiments

In a T-shift experiment, the system is quenched to the initial temperature $T_i (< T_g)$, where it is aged a certain time t_w; the temperature is changed to the measurement temperature $T_m = T_i + \Delta T$, and ZFC-relaxation $M(t)$ (or ac susceptibility relaxation) is recorded. Conjugate experiments with T_i and T_m being interchanged are called *twin* T-shift experiments (see Fig. 5).

The effective age (t_{eff}) of the SG system at T_m, due to the previous aging at T_i, can be determined either from the maximum in the relaxation rate $S(t) = h^{-1} dM(t)/d \log t$ of ZFC relaxation measurements[28,65,66] or by the amount of time that an ac susceptibility-relaxation curve measured after a T shift, needs to be shifted to merge with the reference-relaxation curve measured without a T shift.[11,24,41] We will here show that both ways to derive t_{eff} are consistent, discuss the experimental limitations that determine the accuracy of the estimations, and indicate in which time window the derived effective age gives nontrivial information. Finally, we will use the extracted t_{eff} data to quantitatively analyze the emergence of the chaos effect.

1. ZFC relaxation after T shifts

The relaxation rate after twin T-shift experiments are shown in Fig. 6 for the two samples. The effective age (t_{eff}) of the system after a T shift is determined from the time t_{peak} corresponding to the maximum in $S(t)$ (see Appendix B 2 for details). The shape of the $S(t)$ curves changes after both negative and positive T shifts; the maximum in $S(t)$ becomes broader with increasing $|\Delta T|$ (and for a certain $|\Delta T|$ also with increasing t_w). Due to this broadening t_{peak} becomes less well defined and thus t_{eff} less accurate. A broadening of $S(t)$ with increasing $|\Delta T|$ is observed for both samples, but it should be noted that the temperature shifts employed for the $Fe_{0.5}Mn_{0.5}TiO_3$ sample are much larger than those for the Ag(11 at% Mn) sample. That the data in Fig. 6 shows an increase of t_{peak} with t_w indicates that the ΔT's are small enough to belong to the weakly perturbed regime, i.e., $L_{T_i}(t_w) \lesssim L_{\Delta T}$. The broadening of the relaxation rate can hence be explained by the weak chaos effect (see Sec. II C); during the aging at T_i ghost domains grow at nearby temperatures up to the overlap length. The interior of these ghost

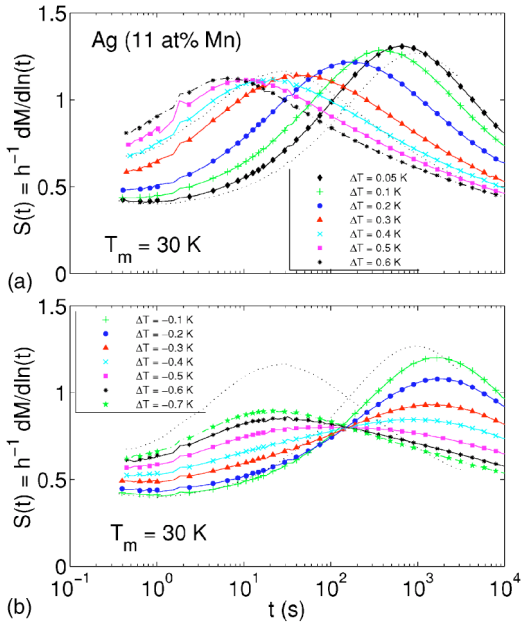

FIG. 7. (Color online) Relaxation rate versus time after aging the Ag(11 at% Mn) sample at (a) T_i=29.95,29.9,29.8,29.7,29.6, 29.5,29.4 K (b) T_i=30.1,30.2,30.3,30.4,30.5,30.6,30.7 K using t_w =1000 s and T_m=30 K. Dotted lines are ordinary isothermal aging curves with t_w=3 and 1000 s. [See Fig. 3 in Ref. 67 for the case of a Cu(Mn) spin glass.]

domains contain defects or noise and do therefore not have full amplitude of the order parameter [Eq. (7)]. These defects are progressively eliminated after the T shift giving rise to extra responses (see Sec. II D). Such extra responses are reflected in the ZFC-magnetization measurements as a broadening of $S(t)$.

For the Ag(11 at% Mn) sample, if $|\Delta T|$ is increased even further, then the maximum in $S(t)$ again becomes narrower, as can be seen in Fig. 7, where positive and negative T shifts with T_m=30 K and t_w=1000 s are shown for various values of T_i. For larger enough $|\Delta T|$ the peak position t_{peak} piles up around t_{min}. This $t_{\text{min}}[L_{\text{min}}=L_T(t_{\text{min}})]$ is the shortest effective age (domain size) in the system after a T change, and it depends on the cooling and/or heating rate as discussed in Sec. II F and Appendix B 2. A similar behavior has been observed in a Cu(Mn) spin glass, as shown in Fig. 3 of Ref. 67. That t_{peak} saturates to t_{min} indicates that $L_{\Delta T}<L_{\text{min}}$; the experimentally accessible times t_w [or lengths $L_{T_i}(t_w)$] lie in the strongly perturbed regime. However, since the overlap length is "hidden" behind the domains grown during the T-change, these measurements do not give any direct information about the overlap length.

For the $Fe_{0.5}Mn_{0.5}TiO_3$ sample the strongly chaotic regime could not be observed within the temperature range used in the experiments reported in the present section. However, we expect to see a narrowing of $S(t)$ also for the $Fe_{0.5}Mn_{0.5}TiO_3$ sample if $|\Delta T|$ is made large enough.

2. ac susceptibility relaxation after T shifts

In an isothermal aging experiment, $\chi''(t)$ is recorded versus time immediately after the quench (only allowing some time for thermal stabilization and stabilization of the ac signal). In a T-shift experiment, $\chi''(t)$ is continuously measured after the initial temperature quench to T_i. In the following we choose $t=0$ immediately after the T shift to T_m.

T-shift ac relaxation measurements with $T_i<T_m$ (positive T shift) are shown in Figs. 8(a) and 8(c). For large enough ΔT, the relaxation curves after the T shifts become identical to the reference isothermal aging curve. The $\Delta T/T_g$ needed to make the aging at the lower temperature negligible is, however, much larger for the $Fe_{0.5}Mn_{0.5}TiO_3$ sample than for the Ag(11 at% Mn) sample. If the time scale of these $\chi''(t)$ curves are shifted by the effective time determined from the corresponding ZFC-relaxation experiments reported before, they merge with the reference isothermal $\chi''(t)$ curve. This is true for both samples [see the insets of Figs. 8(a) and 8(c)], however, a transient part of the curves at short times lies below the isothermal aging curve.

T-shift ac-susceptibility relaxation measurements with $T_i>T_m$ (negative T shift) are shown in Figs. 8(b) and 8(d). For the Ag(11 at% Mn) sample, the T-shift relaxation curves lie below the reference isothermal aging curve for small $|\Delta T|$. However for larger $|\Delta T|$ the T-shifted relaxation curves lie above the reference curve, and for large-enough $|\Delta T|$, the relaxation curves are identical to the isothermal aging curve (complete rejuvenation). For the $Fe_{0.5}Mn_{0.5}TiO_3$ sample, no complete rejuvenation can be observed even for ΔT =−3 K($\Delta T/T_g$=−0.14), whereas for the Ag(11 at% Mn) sample complete rejuvenation is already observed for $|\Delta T|/T_g \gtrsim 0.03$ on the examined time scales. Shifting the time scale by t_{eff}, determined from ZFC-relaxation experiments, makes the T-shift curve merge with the reference curve at long time scales as shown in the insets of the figures. At short time scales, a long transient relaxation exists during which $\chi''(t)$ lies above the reference curve.

The transient part of the susceptibility $\Delta\chi''$ shows nonmonotonic behavior with increasing ΔT in the case of negative T shifts; $\Delta\chi''$ initially becomes larger but it eventually disappears for large ΔT's as $t_{\text{eff}}\to 0$. These two features can be observed for the Ag(11 at% Mn) sample in Fig. 8(b) and complete rejuvenation ($t_{\text{eff}}=0$ and $\Delta\chi''=0$) is shown in Fig. 4. However, only the initial increase of $\Delta\chi''$ can be observed for the $Fe_{0.5}Mn_{0.5}TiO_3$ sample in Fig. 8(d). The nonmonotonic behavior of $\Delta\chi''$ is consistent with the picture presented in Sec. II D, in the weakly perturbed regime, the excess transient responses should be proportional to ΔT and the duration of the transient response t_{trans} is roughly the same as the effective time t_{eff}, while in the strongly perturbed regime $\Delta\chi''\to 0$ as $t_{\text{eff}}\to 0$, which is the limit of complete rejuvenation.

3. Nonaccumulative aging

The previous sections described how to determine the effective age (t_{eff}) of the SG systems after a T-shift. The extracted effective age can now be used to examine if the aging is fully accumulative or not. The advantage of the twin T-shift method[28] is that it allows one to distinguish between the two cases although the growth law $L_T(t)$ is unknown. By plotting t_2 (t_w or t_{eff} at T_2) versus t_1 (t_w or t_{eff} at T_1), the sets of data from the positive T shifts and the corresponding

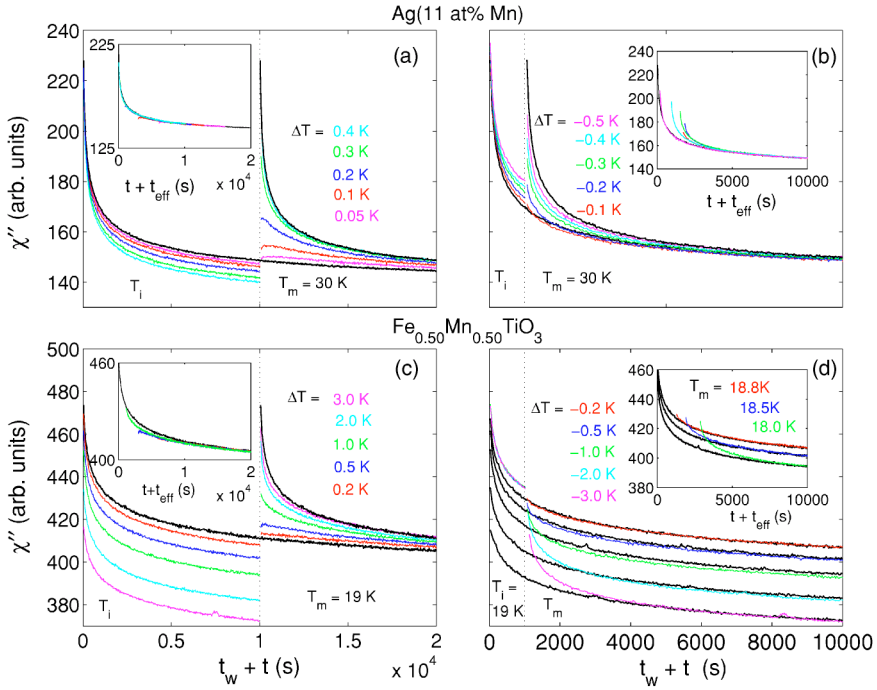

FIG. 8. (Color online) χ'' versus time measured for positive and negative T-shift experiments. (a) The Ag(11 at% Mn) sample is aged at T_i=29.95,29.9,29.8,29.7,29.6 K for t_w=10 000 s before changing the temperature to T_m=30 K. (b) It is aged at T_i=30.1,30.2,30.3,30.4, 30.5 K for t_w=1000 s before changing the temperature to T_m=30 K. (c) The $Fe_{0.5}Mn_{0.5}TiO_3$ sample is aged at T_i=18.8,18.5,18.0,17.0, 16.0 K for t_w=10 000 s before changing the temperature to T_m=19 K. (d) It is aged at T_i=19 K for t_w=1000 s before changing the temperature to T_m=18.8,18.5,18.0,17.0,16.0 K. The thick lines are the (reference) isothermal aging curves starting from $t_w+t=0$ and $t_w+t=t_w$. The insets show $\chi''(T_m)$ versus $t+t_{\rm eff}$ with $t_{\rm eff}$ determined from ZFC-relaxation experiments. f=510 mHz.

negative T shifts should fall on the same line corresponding to $t_2=L_{T_2}^{-1}[L_{T_1}(t_1)]$ if the aging is fully accumulative, while any deviation suggests emergence of rejuvenation (nonaccumulative aging).

Plots of t_1 versus t_2 are shown in Fig. 9. $t_{\rm eff}$ is determined from the twin T-shift ZFC-relaxation experiments shown in Fig. 6. For the Ag(11 at% Mn) sample, the line of accumulative aging is shown in addition; a logarithmic domain growth law [Eq. (A2)] has been used with parameters taken from previous studies.[28,29] It can be seen for both samples that the aging is accumulative for small values of $|\Delta T|$ while for larger $|\Delta T|$ nonaccumulative aging is observed (the data for positive and negative T shifts do not any longer fall on the same line). There is, however, a large difference between the two samples as to how large values of $|\Delta T|/T_g$ are required to introduce nonaccumulative aging. A similar analysis of $t_{\rm eff}$ after twin T-shift experiments was recently performed on the 3D EA Ising model.[41] Only very weak rejuvenation effects could be observed for the Ising model on the time and length scales accessible by the numerical simulations even for such large $\Delta T/T_g$ as 0.3.

4. Evidence for temperature-chaos

Is the nonaccumulative aging consistent with temperature chaos as predicted by the droplet model? In order to answer that question we need to transform time scales into length scales. In other words, we need to know the functional form of the domain growth law. In Ref. 29 it was shown that the ac relaxation data measured at different frequencies and temperatures are consistent with a logarithmic domain growth law [Eq. (A2)]. The temperatures used in that study include those in Fig. 6 for the Ag(11 at% Mn) sample, but not for the $Fe_{0.5}Mn_{0.5}TiO_3$ sample. We therefore restrict the search of temperature chaos to the Ag(11 at% Mn) sample.

For the Ag(11 at% Mn) sample, we showed in Ref. 28 that positive and negative twin T shifts can be made equivalent by plotting $L_{T_m}(t_{\rm eff})$ versus $L_{T_i}(t_w)$. This supports the expectation of the droplet theory[16,17] that there is a unique overlap length between a given pair of temperatures. By scaling $L_{T_m}(t_{\rm eff})$ and $L_{T_i}(t_w)$ with the overlap length $L_{\Delta T}=L_0(a|\Delta T|/T_g)^{-1/\zeta}$, all data corresponding to different T_i, T_m, and t_w merge on a master curve if $1/\zeta$=2.6 (see Fig. 10). This master curve is consistent with the scaling ansatz in the weakly perturbed regime [Eqs. (9)–(11)] as shown in the figure.

In the limit of strong chaos it is theoretically expected that $L_{T_m}(t_{\rm eff})=L_{\Delta T}$ [Eqs. (9) and (12)] and, hence, that the effective age of the system should only be given by the overlap length $L_{\Delta T}$ and not by the wait time t_w. Our study is, however, strongly limited by the experimental time window. The upper limit 10^4–10^5 s is set by how long we can wait for our experiments to finish, while the lower limit $t_{\rm min}$ is set by the cooling and/or heating rate and the time needed to stabilize the temperature (see Appendix B 2). For large $\Delta T \gtrsim 0.7$, $t_{\rm peak}$ is saturated to $t_{\rm min}$ (corresponding to $L_{\rm min}$) and, obviously, such values of $t_{\rm peak}$ cannot be used in the scaling

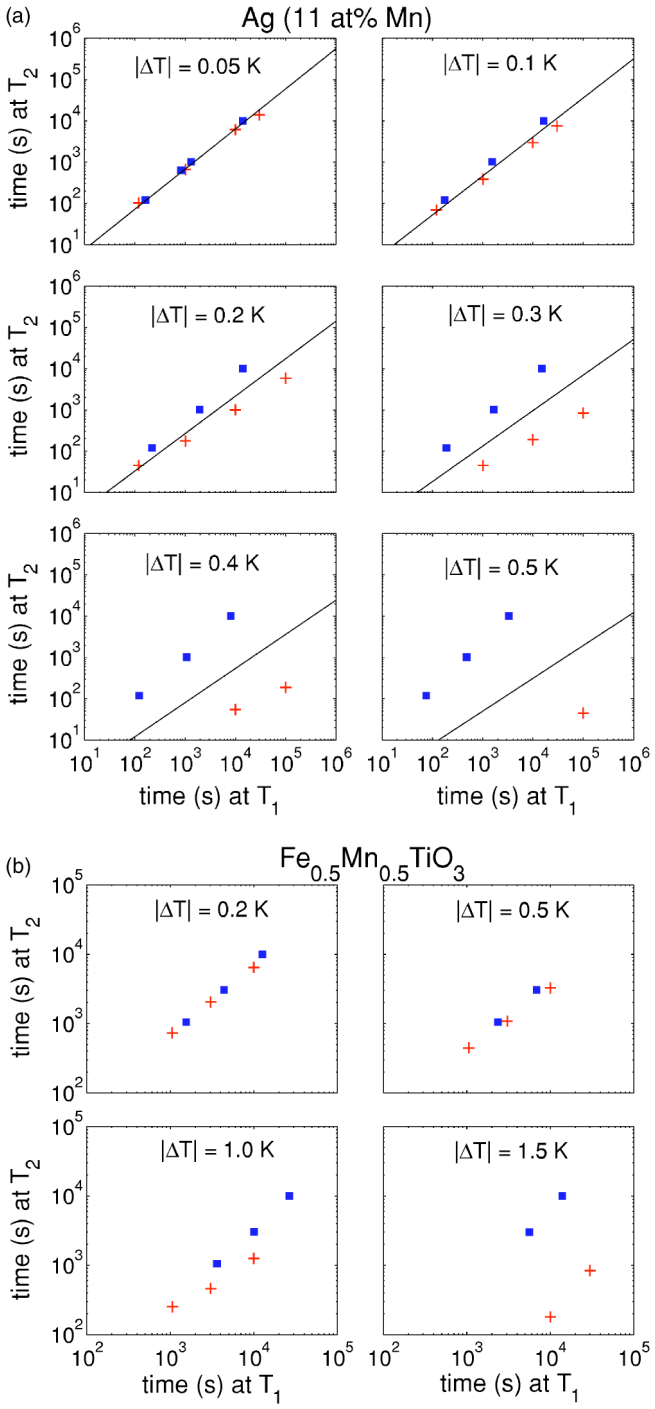

FIG. 9. (Color online) Relation between t_w and $t_{\rm eff}$ in twin experiments: (T_1,T_2) shown as pluses and (T_2,T_1) shown as squares. (a) For the Ag(11 at% Mn) sample, $T_1=(30-|\Delta T|)$ K and $T_2=30$ K with $|\Delta T|=0.05,0.1,0.2,0.3,0.4,0.5$ K $(0.015T_g)$. The solid line indicates fully accumulative aging $L_{T_1}(t_1)=L_{T_2}(t_2)$, calculated assuming logarithmic domain growth [Eq. (A2)]. (b) for the $Fe_{0.5}Mn_{0.5}TiO_3$ sample, $T_1=(19-|\Delta T|)$ K and $T_2=19$ K with $|\Delta T|=0.2,0.5,1.0,1.5$ K $(0.064T_g)$.

plot in Fig. 10. $L_{\Delta T}$ cannot be observed directly in this regime, but the fact that $L_{\Delta T}<L_{\rm min}$, in and of itself, gives evidence for strong chaos within the experimental time (length) window.

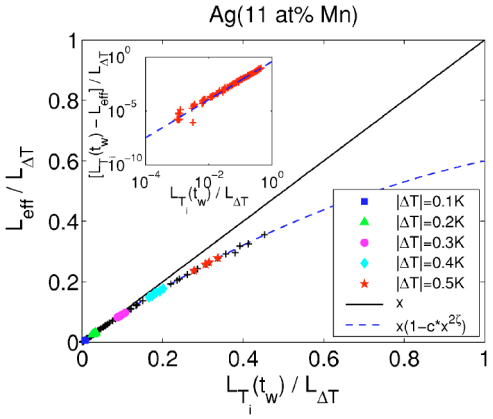

FIG. 10. (Color online) Scaling plot of $L_{\rm eff}$ with $L_{\Delta T}=L_0(a|\Delta T|/T_g)^{-1/\zeta}$ with $a=6$ and $1/\zeta=2.6$. The fit is due to the scaling ansatz for the weakly perturbed regime [Eq. (11)] with $c=0.4$. The deviation from accumulative aging is shown in the inset, and the line is the fit to the scaling ansatz for the weakly perturbed regime. (See Fig. 12 for the corresponding scaling plot of the data of bond shifts in the 4D EA model.)

Finally, we will make some comments on the validity of the scaling presented in Fig. 10. The quality of the scaling does not change significantly when altering the values of the parameters ($\tau_m=10^{-13}$ s, $T_g=32.8$ K, $z\nu=7.2$, $\psi=1.2$, $J=T_g$, and $\nu=1.1$ from Ref. 28), with one exception—symmetry between positive and negative T shifts is obtained only if $\psi\nu\approx 1.3$. The x and y scale are completely arbitrary. We have intentionally chosen the constant a so that the data appear to be rather close to the strong chaos regime.

B. Bond-shift simulations

We now present results of bond-shift simulations on the $\pm J$ EA model introduced in Sec. II A. Two sets of bonds $\mathcal{J}_A$ and $\mathcal{J}_B$ are prepared as explained in Sec. II B. Namely, the set of bonds $\mathcal{J}_B$ is created from the set $\mathcal{J}_A$ by changing the *sign* of a small fraction p of the bonds randomly. The protocol of the simulation is the following: a system with a certain set of bonds $\mathcal{J}^A$ is aged for a time t_w, after which the bonds are replaced by $\mathcal{J}^B$, and the relaxation of the spin autocorrelation function

$$C_{\rm ZFC}(t+t_w,t_w)=(1/N)\sum_i \langle S_i(t_w)S_i(t+t_w)\rangle, \qquad (23)$$

where i runs over the N Ising spins S_i in the system, is recorded. The brackets $\langle\ldots\rangle$ denote the averages over different realizations of initial conditions, thermal noises, and random bonds. The subscript "ZFC" is meant to emphasize that this autocorrelation function is conjugate to the ZFC susceptibility: if the fluctuation dissipation theorem (FDT) holds $[1-C_{\rm ZFC}(t)](J/T)$ becomes identical to the ZFC susceptibility. The relaxation rate $S(t)$ is extracted by computing the logarithmic derivatives numerically,

$$S(t)=-dC_{\rm ZFC}(t+t_w,t_w)/\log(t). \qquad (24)$$

Usually the ZFC susceptibility is used to obtain the relaxation rate. Here, we used the autocorrelation function be-

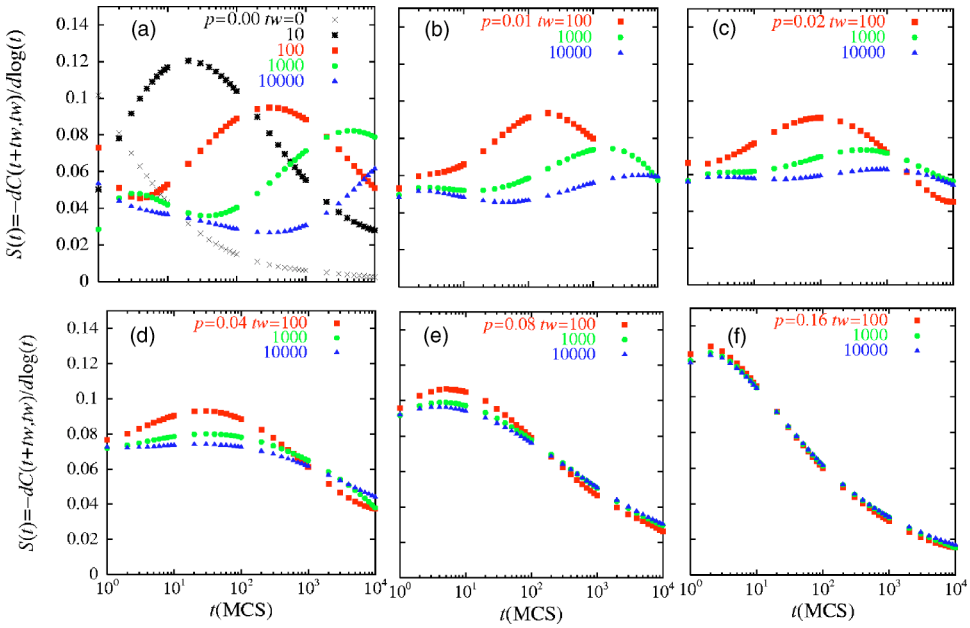

FIG. 11. (Color online) The relaxation rate $S(t)=-dC(t+t_w,t_w)/\log(t)$ of the 4D EA model after different waiting times t_w with bond shifts of various strength p at temperature $T=0.6T_g$.

cause it has much less statistical fluctuations. We note that FDT is well satisfied within what is called the quasiequilibrium regime[63] so that $S(t)$ defined above yields almost the same effective time $t_{\rm eff}$ as obtained from the ZFC susceptibility. We remark that the autocorrelation function can be measured experimentally by a noise-measurement technique.[68]

In Fig. 11, we show some data of relaxation rates obtained at $T/J=1.2$ ($T/T_g=0.6$) for bond-shift simulations with wait times $t_w=10^2, 10^3, 10^4$, and various strength of the perturbations $\Delta J/J\sim\sqrt{p}$ with p in the range of 0–0.16. For relatively small $p(\lesssim 0.05)$, it can be seen that the peaks in the relaxation rate $S(t)$ become *broader* either by increasing p or t_w. Simultaneously, with increasing p, they become somewhat suppressed and their positions are slightly shifted to shorter times compared to the peaks of the reference curves for $p=0.0$ [Fig. 11(a)]. At larger $p(\gtrsim 0.05)$, different features can be noticed. The relaxation rate $S(t)$ still becomes broader by increasing t_w, but tends to saturate to some limiting curve. By increasing the strength of perturbation p further, not only the peak position of $S(t)$ is shifted to shorter times, but the shape of $S(t)$ again becomes *narrower*. Remarkably, these features are very similar to experimental data where ΔT is varied. The effects of temperature perturbations shown in Fig. 6 showed considerable broadening of $S(t)$ while Fig. 7 showed narrowing of $S(t)$.

The results can be qualitatively interpreted according to the picture presented in Sec. II D. We know that the dynamical length scales $L_T(t)$ do not vary much within the feasible range of time scales t_w (see Fig. 24), while the overlap length $L_{\Delta J}(p)\propto\sqrt{p}^{-1/\zeta}$ given in Eq. (4) varies appreciably with the strength of the perturbation p. The saturation of the t_w dependence can be interpreted to show that with large enough p the strongly perturbed regime of the chaos effect enters the numerical time (length) window. The *broadening* of $S(t)$ suggests that the order parameter [Eq. (7)] does not have its full amplitude; in other words, the domains are noisy or ghostlike. This noise is progressively eliminated, starting from the small defects and giving rise to the excessive response, as discussed in Sec. II D. On the other hand, the *narrowing* of $S(t)$ at larger $p(>0.05)$ suggests that the overlap length $L_{\Delta J}(p)$ has become smaller than $L_T(t_w)$ and even approaches the minimum length scale $L_0\sim 1$. Thus the excessive response decreases as the effective domain size [Eq. (9)] is reduced with increasing p and finally disappears in the strongly perturbed regime. Interestingly, this behavior resembles the results from our T-shift experiments on the Ag(11 at% Mn) sample. There, a considerable narrowing of the peak in $S(t)$ occurred for large temperature shifts $\Delta T\gtrsim 0.6$ K (see Fig. 7), from which we concluded that the overlap length had become as small as the lower limit $L_{\rm min}$ induced by the finiteness of the heating and/or cooling rate and the time required to stabilize a temperature in experiments.

Let us turn to a more quantitative analysis similar to that of the temperature perturbation results on Ag(11 at% Mn) in Fig. 10. We first determine the effective time $t_{\rm eff}$ from the peak position $t_{\rm peak}$ of $S(t)$ (see Ref. 70 for details). Then the effective domain size is obtained as $L_{\rm eff}=L_T(t_{\rm eff})$, using the data of the dynamical length $L_T(t)$ obtained in Refs. 63 and 69 to convert time scales to length scales (see Fig. 24). The overlap length was calculated from $L_{\Delta J}(p)/L_0=0.1\sqrt{p}^{-1/\zeta}$ [Eq. (4)] assuming the chaos exponent to be $\zeta=0.9$. The value of the chaos exponent ζ of the present 4D EA Ising model reported in earlier works varies as 0.85 (Ref. 37) and 1.3 (Refs. 71). Here we assume $\zeta=0.9$, but small variations of the chaos exponent do not significantly affect the results reported below.

We are now in position to examine the theory presented in Secs. II C and II D. Equation (9) suggests that all data should collapse onto a master curve by plotting $L_{\rm eff}/L_{\Delta J}(p)$ versus $L_T(t_w)/L_{\Delta J}(p)$. Figure 12 shows the resulting scaling plot. The scaling works perfectly well, including all data from the two different temperatures $T/J=1.2$ and 0.8 at $p<0.05$, which implies that the data collapse on a universal master curve. A fit according to the scaling ansatz for the weakly

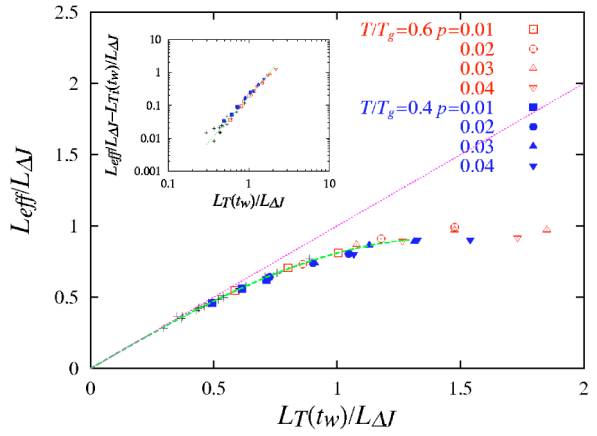

FIG. 12. (Color online) Test of the scaling of $L_{\rm eff}$ after bond shifts in the 4D EA model. The straight line in the main figure is the no-chaos limit. The fit is due to the scaling ansatz for the weakly perturbed regime [Eq. (9)] with $L_{\Delta J}(p)=0.1\sqrt{p}^{-1/\zeta}$ with $\zeta=0.9$. The dynamical length $L_T(t)$ is due to the data obtained in Refs. 63 and 69. Thus, there are essentially zero fitting parameters. The correction part to the no-chaos limit is shown in the inset, where the straight line is the power law with exponent 2ζ. See the corresponding scaling plot in the case of the temperature-shift experiments on the Ag(11 at% Mn) sample shown in Fig. 10.

perturbed regime $L_T(t_w)/L_0 \ll L_{\Delta J}(p)$ is also shown. The correction part $L_{\rm eff}/L_{\Delta J}(p)-L_T(t_w)/L_{\Delta J}(p)$ to the accumulative limit is plotted in the inset. It can be seen that the correction term is proportional to $[L_T/(t_w)L_{\Delta J}(p)]^{2\zeta}$ with $\zeta=0.9$, which is in perfect agreement with the expected scaling behavior for the weakly perturbed regime $L \ll L_{\Delta J}(p)$ [see Eq. (11)]. In the above scaling plot we excluded data for $p>0.05$ where $t_{\rm eff}$ has become too small. As was shown in Fig. 11, $S(t)$ becomes *narrower* at these larger values of p, which suggests that the lower limit of the length scales L_0 now comes into play explicitly. The scaling ansatz Eqs. (9)–(12) should *not* work in such a regime.

V. TEMPERATURE AND BOND CYCLINGS

In this section we will investigate the "memory" that survives even under strong temperature or bond perturbations.

A. Temperature-cycling experiments

In Sec. IV A we found strong evidence that for the Ag(11 at% Mn) sample, our experimental time window lies in the strongly perturbed regime, i.e., $L_{\Delta T}<L_{\rm min}$, in the case of large-enough temperature shifts ($|\Delta T| \gtrsim 1$ K). For the $Fe_{0.5}Mn_{0.5}TiO_3$ sample, on the other hand, the strongly perturbed regime was not reached within the temperature range and time window of our experiments. With this knowledge in mind, we can, for the Ag(11 at% Mn) sample, focus on how the SG *heals* after a negative T cycling into the strongly perturbed regime and make comparisons to the ghost domain scenario presented in Sec. II.

1. One-step temperature cycling

In one-step temperature cycling experiments (see Fig. 13), the sample is first cooled to T_m and aged there a time t_{w_1}; the

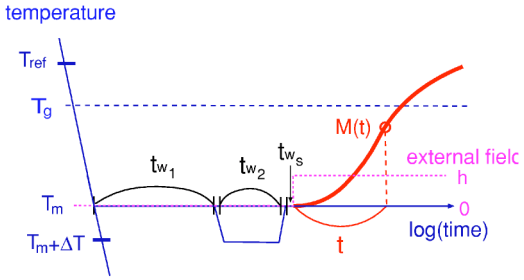

FIG. 13. (Color online) Schematic representation of a one-step temperature-cycling experiment according to the protocol $T_m(t_{w_1}) \rightarrow T_m+\Delta T(t_{w_2}) \rightarrow T_m$. When returning to T_m, a short waiting time, $t_{ws}=3$ s is needed before applying the magnetic field and recording the ZFC relaxation in order to ensure thermal stability. In ac experiments, $\chi(t)$ is also recorded during the cycling.

temperature is subsequently changed to $T_m+\Delta T$, where the sample is aged for a time t_{w_2} (perturbation stage); and then the temperature is put back to T_m (healing stage). After a short wait time t_{ws} to ensure thermal stability at T_m, the magnetic field is switched on and the magnetization $M_{\rm ZFC}(t)$ is recorded, or the ac susceptibility is recorded continuously during the cycling process.

A negative one-step T-cycling experiment ($\Delta T=-2$ K) measuring the out-of-phase component of the ac susceptibility is shown in Fig. 4. Results of such measurements with $t_{w_1}=3000$ s are shown in Fig. 14. The aging at $Tm+\Delta T$ has been cut away in this figure, and only the aging at T_m is shown. It can be clearly seen that the aging at $T_m+\Delta T$ introduces a considerable amount of excessive response, which increases with increasing t_{w_2}. In the ghost domain scenario, the excessive response is attributed to the introduction of noise in the ghost domains by the aging at the temperature $T+\Delta T$. This yields a reduction of the order parameter [cf. Eq. (17)] so that the recovery time $t_{\rm rec}$ corresponds to the time scale at which the order parameter is recovered, and

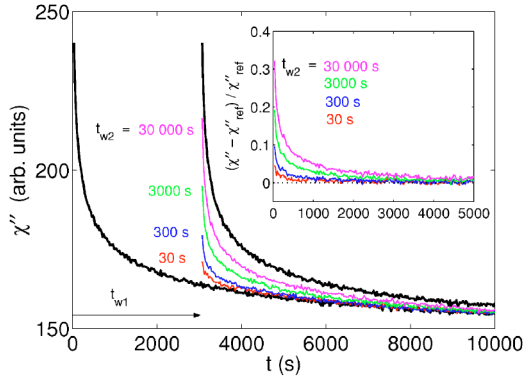

FIG. 14. (Color online) $\chi''(t)$ versus time at T_m for experiments with a negative T cycling of $\Delta T=-2$ K ($T_m+\Delta T=28$ K); $t_{w_1}=3000$ s and $t_{w_2}=30,300,3000,30\,000$ s (bottom to top). The thick (black) lines represent the reference isothermal aging at T_m; one of these curves is shifted a quantity t_{w_1} in time. The inset shows $[\chi''(t)-\chi''_{\rm ref}(t)]/\chi''_{\rm ref}(t)$ for the transient part of the susceptibility after the T cycling. $\chi''(t)$ during the all stages of the T cycling are shown in Fig. 4 for $t_{w_2}=3000$ s. $\omega/2\pi=510$ mHz.

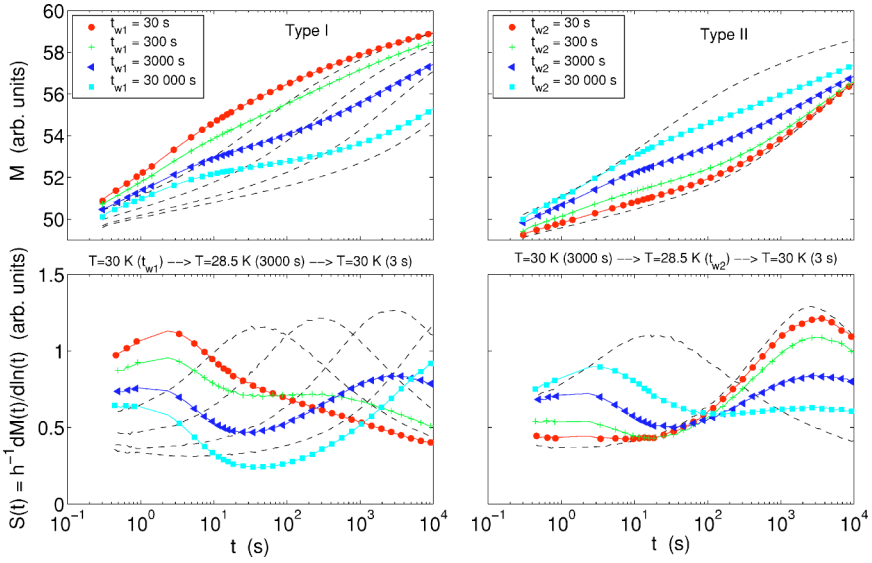

FIG. 15. (Color online) ZFC-relaxation curves [$M_{\mathrm{ZFC}}(t)$ and $S(t)$] obtained after a negative T cycling of $\Delta T=-1.5$ K ($T_m=30$ K; $T_m+\Delta T=28.5$ K); Type I: $t_{w_1}=30,300,$ 3000, and 30 000 s and $t_{w_2}=3000$ s; Type II: $t_{w_1}=3000$ s and $t_{w_2}=30,300,3000,$ 30 000 s. Isothermal aging recorded at $T_m=30$ K are added for comparison in dashed lines; Type I: $t_w=t_{w_1}$, Type II: $t_w=3$ s, and $t_w=3000$ s. (See Fig. 18 for the corresponding data of the one-step bond cycling in the 4D EA model.)

hence, the excessive susceptibility disappears [cf. Eq. (20)]. From Fig. 14, the recovery times t_{rec} are found to be of order $O(10^3$–$10^4)$ s. If the T cyclings would have kept the system in the weakly perturbed regime, the recovery times would become $t_{\mathrm{rec}}^{\mathrm{weak}}=0.04,0.1,0.3,0.9$ s for $t_{w_2}=30,300,3000,30\,000$ s according to Eq. (15) and the growth law Eq. (A2) with the same parameters as in Sec. IV A 4. Consistent with the prediction in Sec. II E 2, the observed values of t_{rec} are several orders-of-magnitude larger than $t_{\mathrm{rec}}^{\mathrm{weak}}$. However, the t_{w_2} dependence of t_{rec} is weaker than expected from Eq. (20) indicating that corrections to the asymptotic formula are important on the experimental length scales.[72] Finally, let us note that a similar observation of anomalously large recovery times was made in a recent study by Sasaki *et al.*[73]

The ZFC magnetization has been measured after negative one-step T cyclings on the Ag(11 at% Mn) sample with $T_m=30$ K and $\Delta T=-1.5$ K. Figure 15 shows the ZFC-relaxation data; Type I: the initial wait time t_{w_1} is varied while the duration of the perturbation $t_{w_2}=3000$ s is fixed. Type II: the initial wait time is fixed to $t_{w_1}=3000$ s while the duration of the perturbation t_{w_2} is varied. Isothermal aging data are also shown in these figures for comparison. As seen in the figures, the magnetization always exhibits an enhanced growth rate at observation times around t_{min} after the cycling, and in addition, a second enhanced growth rate at observation times around t_{w_1}, which are manifested as two peaks in the relaxation rate $S(t)$. The peak of $S(t)$ around t_{min} can be attributed to rejuvenation effects, and the peak around t_{w_1} to memory effects. It can be seen that by increasing the duration of the perturbation t_{w_2}, the height of the second peak of $S(t)$ at around t_{w_1} dramatically decreases, but the peak position itself does not change appreciably. By studying the magnetization curve and comparing it to the reference curve of isothermal aging (with wait time $t_w=t_{w_1}$), it can be appreciated that the cycling data eventually merges with that of the isothermal aging curve (although it is outside the time scales of our measurements). The time scale of the merging appears to become larger for longer duration of the perturbation t_{w_2}.

Within the ghost-domain picture discussed in Sec. II, this two-stage enhancement of the relaxation rate can be understood as follows. The aging at the second stage introduces strong noise and reduces the amplitude of the order parameter in the ghost domains $L_{T_m}(t_{w_1})$ grown at T_m during the initial aging. The system is hence strongly disordered with respect to the equilibrium state at T_m, but the original domain structure is conserved as a bias effect (the order parameter $\rho_{\mathrm{rem}}>0$). During the third stage (healing stage) the aging called inner-coarsening starts, i.e., new domain growth starting from an almost random state although with a weakly biased initial condition. Hence, when the magnetic field is switched on in the healing stage, the inner-coarsening has already proceeded for the time t_{min}. This is reflected by the first peak of $S(t)$. During the healing stage, the strength of the bias keeps increasing so that the noise (minority phases) within ghost domains is progressively removed. The second peak of $S(t)$ corresponds to the size of the ghost domain $L_{T_m}(t_{w_1})$, which itself continues to slowly expand in the healing stage (outer coarsening). Thus, this represents the memory of the thermal history before the perturbation. An illustration of this noise-imprinting-healing scenario is given in Fig. 2. However, the increase of the bias is so slow that the recovery time $t_{\mathrm{rec}}^{\mathrm{strong}}$ of the order parameter can be extremely large as given in Eq. (20). Then, the order parameter within a ghost domain may not be recovered fully until the ghost domain itself has grown appreciably in the healing stage. Probably this explains the fact that the second peak of $S(t)$ is greatly suppressed (but not erased) by increasing the duration of the perturbation t_{w_2}, which also increases the recovery time $t_{\mathrm{rec}}^{\mathrm{strong}}$.

2. Two-step temperature cycling

Finally, two-step T cyclings are studied in order to investigate the anomalous multiplicative effects of noise anticipated by the ghost domain picture [see Sec. II E 3]. In this protocol, an extra T shift is added to the one-step temperature-cycling procedure shown in Fig. 13; the sample is cooled to T_m where it is aged a wait time t_{w_1} (initial aging stage), subsequently the temperature is shifted to $T_1=T_m+\Delta T_1$ for a time t_{w_2} (first perturbation stage), then shifted to

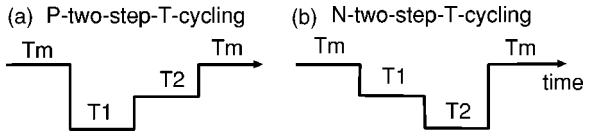

FIG. 16. Schematic illustration of (a) positive $(T_2 > T_1)$ and (b) negative $(T_2 < T_1)$ two-step T cycling.

$T_2 = T_m + \Delta T_2$ for a time t_{w_3} (second perturbation stage), and finally, changed back to T_m (healing stage) where $M_{\mathrm{ZFC}}(t)$ is recorded. As illustrated in Fig. 16 one can make two different kinds of two-step-T-cycling experiments (with $T_1, T_2 < T_m$); involving either a positive $(T_2 > T_1)$ or a negative $(T_2 < T_1)$ T-shift between T_1 and T_2.

In Fig. 17, a set of data using the two-step temperature-cycling protocol with $T_m = 30$ K and $t_{w_1} = t_{w_2} = t_{w_3} = 3000$ s are shown, together with reference data for one-step cycling experiments and isothermal aging experiments at T_m. It can be seen that the data of the N-two-step experiment with $(T_1, T_2) = (29\ \mathrm{K}, 27\ \mathrm{K})$ is slightly more rejuvenated than the corresponding one-step cycling with $T_m + \Delta T = 29$ K and $t_{w_2} = 3000$ s, while the data of the P-two-step experiment with $(T_1, T_2) = (27\ \mathrm{K}, 29\ \mathrm{K})$ is much more rejuvenated. Furthermore, the data of the P-two-step experiment with $(T_1, T_2) = (28\ \mathrm{K}, 29\ \mathrm{K})$ is strikingly more rejuvenated, so that the

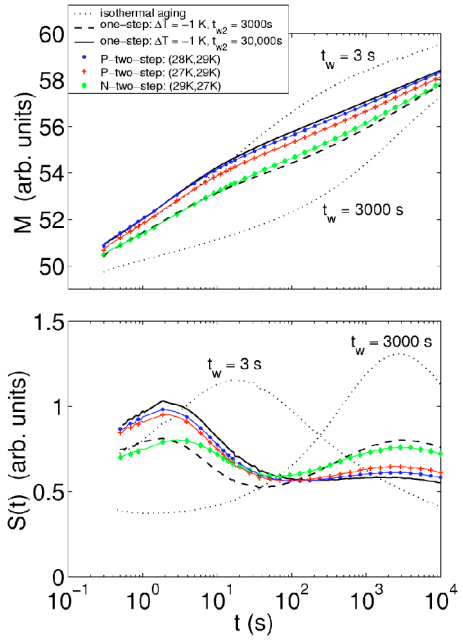

FIG. 17. (Color online) ZFC-relaxation curves obtained after negative two-step T cyclings. Two-step T-cycling experiments $T_m(t_{w_1}) \rightarrow T_1(t_{w_2}) \rightarrow T_2(t_{w_3}) \rightarrow T_m$ with $T_m = 30$ K and $t_{w_1} = t_{w_2} = t_{w_3} = 3000$ s are shown. A negative T shift in $T_1 \rightarrow T_2$ is made with $(T_1, T_2) = (29\ \mathrm{K}, 27\ \mathrm{K})$ (diamonds), and positive T shifts in $T_1 \rightarrow T_2$ are made with $(T_1, T_2) = (28\ \mathrm{K}, 29\ \mathrm{K})$ (circles), $(T_1, T_2) = (27\ \mathrm{K}, 29\ \mathrm{K})$ (pulses). The isothermal aging with $t_w = 3$ and 3000 s (dotted lines) at $T_m = 30$ K and one-step T-cycling experiments $T_m(t_{w_1}) \rightarrow T_m + \Delta T(t_{w_2}) \rightarrow T_m$ with $T_m = 30$ K, $T_m + \Delta T = 29$ K, $t_{w_2} = 3000$ and 30 000 s (dashed lines) are shown for comparison. (See Fig. 19 for the corresponding data of the two-step bond cycling in the 4D EA model.)

$M_{\mathrm{ZFC}}(t)$ curve is close the one-step cycling with $T_m + \Delta T = 29$ K and $t_{w_2} = 30\,000$ s. This may appear surprising, since the total duration of the actual perturbation is only $t_{w_2} + t_{w_3} = 6000$ s.

The anomalously strong rejuvenation effect after the two-step cycling can be understood by the ghost domain picture as the multiplicative effect of noise given in Eq. (22). One should, however, take into account the renormalization of the overlap length $L_{\Delta T} \rightarrow L_{\min}(v_T, T)$ due to finiteness of heating and/or cooling rates discussed in Sec. II F. Naturally, the latter effect can significantly or even completely hide the multiplicative nature of the noise introduction, as appears to have happened in a previous study.[23] To reduce such "disturbing" effects as much as possible, one should use fast-enough heating and cooling rates. It should also be recalled that in the present experiments, the heating is almost 10 times faster than cooling, which implies that the renormalized overlap length $L_{\min}(v_T, T)$ is larger for cooling than for heating. This may explain the apparent asymmetry of the negative and positive two-step T cyclings in Fig. 17. The weaker rejuvenation effect observed in the P-two-step measurement $(T_1, T_2) = (27\ \mathrm{K}, 29\ \mathrm{K})$ compared with (28 K, 29 K) can simply be attributed to the temperature dependence of the domain growth law Eq. (A2).

B. Bond-cycling simulations

1. One-step bond cycling

For a one-step bond-cycling simulation on the $\pm J$ EA model, we prepare two sets of realizations of interaction bonds $\mathcal{J}^A$ and $\mathcal{J}^B$ as before. The set of bonds $\mathcal{J}_B$ is created from $\mathcal{J}_A$ by changing the *sign* of a small fraction p of the latter randomly. In order to work in the strongly perturbed regime we choose $p = 0.2$, since the analysis in the previous section (see Fig. 12) ensures that almost the whole time window of the simulations lies well within the strongly perturbed regime with $p = 0.2$. We also made simulations with the weaker strength of the perturbation $p = 0.05$, for which time scales greater than 10^3 MCS belongs to the strongly perturbed regime as can be seen in Fig. 12 and obtained qualitatively the same results, but with larger statistical errors. The working temperature is fixed to $T/T_g = 0.6$ throughout the simulations and the strength of the probing field is $h/J = 0.1$, which is small enough to observe linear response within the present time scales.[63]

The procedure of the one-step bond cycling is as follows. First, the system is let to evolve under $\mathcal{J}^A$ for a time t_{w_1} at temperature T starting from a random-spin configuration. Then, the bonds are replaced by $\mathcal{J}^B$, and the system is let to evolve another time interval t_{w_2}. Finally, the bonds are put back to $\mathcal{J}^A$, and the system is let to evolve. After a time interval t_{w_3}, a small magnetic field h is switched on and the growth of the magnetization is measured to obtain the ZFC susceptibility

$$\chi_{\mathrm{ZFC}}(t) = (J/h)(1/N)\sum_i \langle S_i(t + t_{w_3} + t_{w_2} + t_{w_1})\rangle \qquad (25)$$

where t is the time elapsed after the magnetic field is switched on. We also measured the conjugate autocorrelation

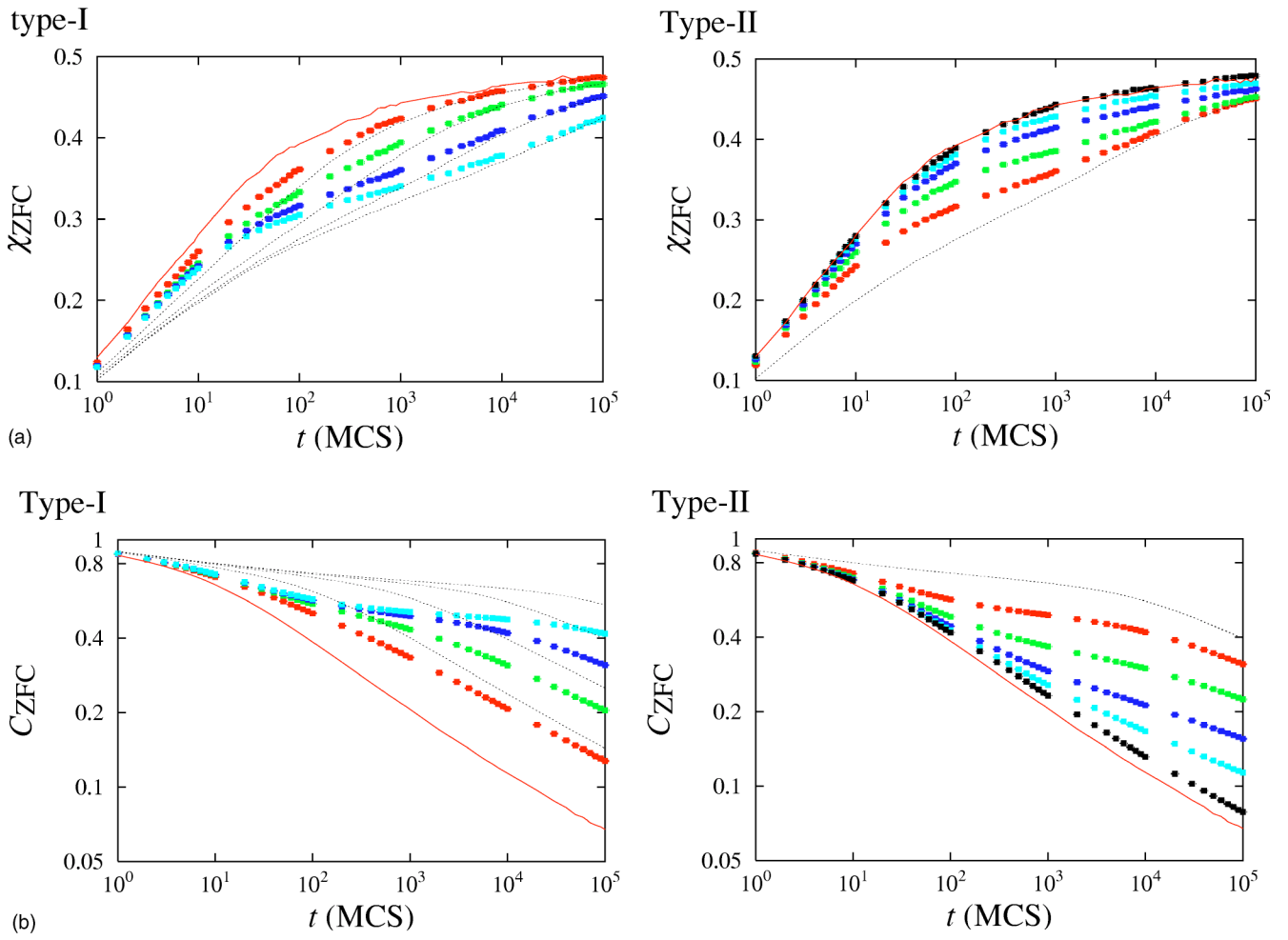

FIG. 18. (Color online) ZFC susceptibility and the corresponding autocorrelation function in the 4D EA model after bond cyclings. The filled squared are the data obtained after bond cyclings with Type I: $t_{w_1}=10^2,10^3,10^4,10^5$ MCS (χ_{ZFC} from top to bottom C_{ZFC} from bottom to top), $t_{w_2}=10$, and $t_{w_3}=10$ (MCS); Type II: $t_{w_1}=10^4$ MCS, $t_{w_2}=10$, 40, 160, 640, and 10^5 MCS (χ_{ZFC} from top to bottom C_{ZFC} from bottom to top), and $t_{w_3}=10$ MCS. The solid lines are the reference isothermal aging data: (a) $\chi_0(t,t_w)$ and (b) $C_0(t,t_w)$ with $t_w=t_{w_3}$ and the dotted lines those with $t_w=t_{w_1}+t_{w_3}$. (See Fig. 15 for the corresponding temperature-cycling experiment.)

function to the ZFC susceptibility in the same protocol but without applying a magnetic field,

$$C_{ZFC}(t) = C(t + t_{w_3} + t_{w_2} + t_{w_1}, t_{w_3} + t_{w_2} + t_{w_1}), \qquad (26)$$

where $C(t_1,t_2)=(1/N)\Sigma_i S_i(t_1)S_i(t_2)$ is the spin autocorrelation function. Again, the subscript "ZFC" is used to emphasize that this autocorrelation function is conjugate to the ZFC susceptibility if the FDT holds. We expect both quantities to reflect the inner and outer coarsening discussed in Sec. II, but there are also apparent differences. First, the FDT is expected to be violated in the outer-coarsening regime.[63] Second, the linear susceptibility $\chi_{ZFC}(t)$ should have the so-called weak long-term memory property,[4] stating that an integral of linear responses during a finite interval of time finally disappears at later times, whereas the autocorrelation does not have such a property.

In Fig. 18, we show a data set labeled "type-I," where the initial wait time t_{w_1} is varied while the other time scales are fixed. Another data set labeled "type-II" is also shown, where the duration of the perturbation t_{w_2} is varied while the other time scales are fixed. The corresponding data in the case of temperature cyclings are shown in Fig. 15. In all of the data in Fig. 18, there is a common feature that the ZFC susceptibility $\chi_{ZFC}(t)$ and the conjugate autocorrelation function $C_{ZFC}(t)$ exhibit two-step relaxation processes that can be naturally understood as the inner and outer coarsening discussed in Sec. II. In the figures the data of the reference isothermal aging without perturbations of the ZFC susceptibility $\chi_0(t,t_w)$ and the autocorrelation function $C_0(t,t_w)$ are shown for comparison.

Quite remarkably, the generic features of the behavior of the ZFC susceptibility $\chi_{ZFC}(t)$ is the same as in temperature-cycling experiments. First, there is an initial growth of the susceptibility that appears to be close to the curve of the reference isothermal aging $\chi_0(t,t_w)$ with wait time $t_w=t_{w_3}$. This feature can be naturally understood to be due to the inner coarsening. Then, there is a crossover to $\chi_0(t,t_w)$ with wait time $t_w=t_{w_1}+t_{w_3}$, which can naturally be understood as due to the outer coarsening.

Correspondingly, and as expected, the autocorrelation function $C_{\mathrm{ZFC}}(t)$ exhibits a similar two-step relaxation as $\chi_{\mathrm{ZFC}}(t)$. It initially follows the reference curve $C_0(t,t_w)$ of $t_w=t_{w_3}$ (inner coarsening) and makes a crossover to slower decay, which depends on $t_{w_1}+t_{w_3}$ (outer coarsening) at later times. This autocorrelation function was studied in bond-cycling simulations of the spherical and Ising Mattis model in Ref. 20 with rejuvenation set in by hand, where essentially the same result as this was obtained. Thus, the present results support that the same mechanism of memory is at work in the spin-glass model.

2. Two-step bond cycling

For the two-step bond cycling, we consider that the procedure $\mathcal{J}^A\rightarrow\mathcal{J}^B\rightarrow\mathcal{J}^C\rightarrow\mathcal{J}^A$ is the same as the one-step bond cycling except that some time t_{w_3} is spent at $\mathcal{J}^C$ before coming back to $\mathcal{J}^A$. The bonds of $\mathcal{J}^A$ and $\mathcal{J}^B$ are prepared as in the one-step cycling case, i.e., the set of bonds $\mathcal{J}^B$ is created from $\mathcal{J}^A$ by a perturbation of strength p. The third set of bonds $\mathcal{J}^C$ is created from $\mathcal{J}^B$ by a perturbation of strength p. Note, that this corresponds to create $\mathcal{J}^C$ out of $\mathcal{J}^A$ by a perturbation of strength $p'=2p(1-p)$. Here, we again use $p=0.2$ and thus $p'=0.32$ in order to work in the strongly perturbed regime. The temperature is again fixed to $T/T_g=0.6$ throughout the simulations and the strength of the probing field is $h/J=0.1$.

In Fig. 19, we show the ZFC susceptibility $\chi_{\mathrm{ZFC}}(t)$ and the conjugate autocorrelation function $C_{\mathrm{ZFC}}(t)$ after the two-step bond cyclings $\mathcal{J}^A\rightarrow\mathcal{J}^B\rightarrow\mathcal{J}^C\rightarrow\mathcal{J}^A$, which is compared with the data of the one-step bond cyclings $\mathcal{J}^A\rightarrow\mathcal{J}^C\rightarrow\mathcal{J}^A$. It can be seen that the effect of the two-step perturbations with $t_{w_2}=t_{w_3}=10$ MCS is stronger than the one-step perturbation with $t_{w_2}=20$ MCS. Moreover, two-step perturbations with $t_{w_2}=t_{w_3}=80$ MCS is as strong as the one step-perturbation with $t_{w_2}=640$ MCS.

The above result can hardly be understood by a naive length-scale argument. It resembles the result of the corresponding two-step temperature-cycling experiments discussed in Sec. V A and is consistent with the expectation in the ghost domain scenario, which predicts multiplicative effects of perturbations in the strongly perturbed regime [see Eq. (22)].

VI. MEMORY EXPERIMENTS

This section discusses memory experiments that probe nonequilibrium dynamics under continuous temperature changes and halts, using low-frequency ac susceptibility and ZFC-magnetization measurements. Such experiments have become a popular tool for investigations of memory and rejuvenation effects in various glassy systems, for example, interacting nanoparticles,[12] polymer glasses,[74] and granular superconductors.[15] It can, however, be difficult to interpret the experiments because memory and rejuvenation effects are mixed with cooling- and/or heating-rate effects in a nontrivial way.

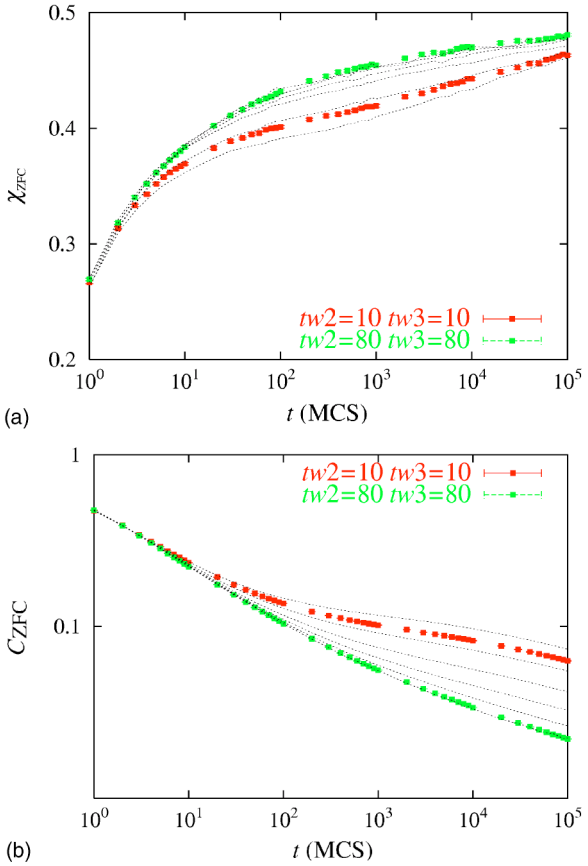

FIG. 19. (Color online) The relaxation after two-step bond cycling $\mathcal{J}^A\rightarrow\mathcal{J}^B\rightarrow\mathcal{J}^C\rightarrow\mathcal{J}^A$. The target equilibrium state is cycled as $\mathcal{J}^A(10^4\ \mathrm{MCS})\rightarrow\mathcal{J}^B(t_{w_2}\ \mathrm{MCS})\rightarrow\mathcal{J}^C(t_{w_3}\ \mathrm{MCS})\rightarrow\mathcal{J}^A(t\ \mathrm{MCS})$. In the figures the dotted lines are the reference data of one-step bond-cycling $\mathcal{J}^A(10^4\ \mathrm{MCS})\rightarrow\mathcal{J}^C(t_{w_2}\ \mathrm{MCS})\rightarrow\mathcal{J}^A(t\ \mathrm{MCS})$ with $t_{w_2}=20$, 40,80,160,320,640 MCS, which vary from bottom to top in (a) and from top to bottom in (b). (See Fig. 17 for the corresponding two-step temperature-cycling experiment.)

A. ac memory

Results of ac-susceptibility memory experiments are shown in Fig. 20; the ac susceptibility is measured on cooling and on the subsequent reheating. Measurements are made both with and without temporary stop(s) at constant temperature on cooling. In the figure, $\chi''(T)$ is plotted versus temperature for the two samples. It is interesting to note that even without a temperature stop, we observe differences between Ag(11 at% Mn) and $Fe_{0.5}Mn_{0.5}TiO_3$ in regard to the relative levels of $\chi''(T)$ measured on cooling and reheating (the "direction" of measurement is indicated with arrows on the figure). In the case of Ag(11 at% Mn), the heating curve lies significantly above the cooling curve (except close to the lowest temperature). Such a behavior can only be explained by strong rejuvenation processes during the cooling and reheating procedure. In the case of $Fe_{0.5}Mn_{0.5}TiO_3$, on the other hand, the susceptibility curve recorded on reheating lies below the corresponding cooling curve, indicating that some equilibration of the system is accumulative in the cooling and reheating process. By making one or two temporary stops during the cooling processes, memory dips are intro-

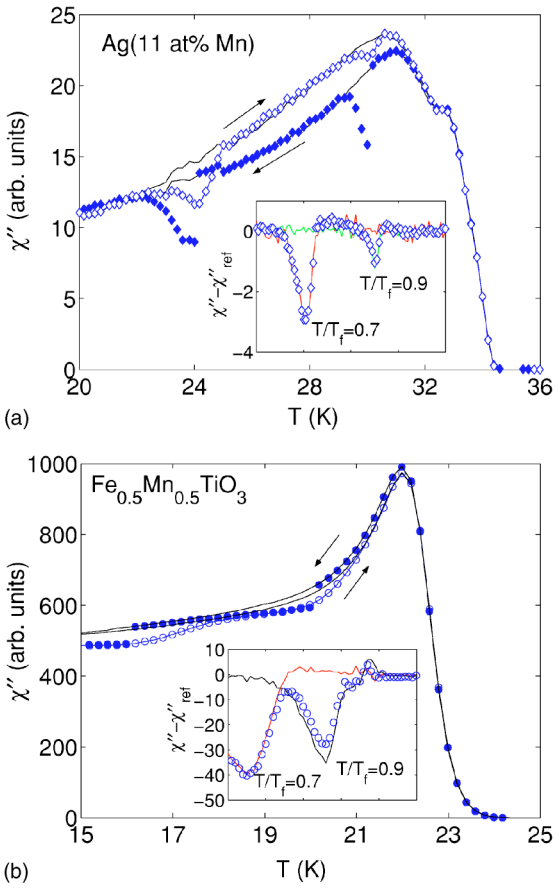

FIG. 20. (Color online) χ'' versus temperature with temporary stops at (a) $T_{s_1}=30$ K and $T_{s_2}=24$ K and (b) $T_{s_1}=20$ K and $T_{s_2}=16$ K; $t_{s_1}=t_{s_2}=3000$ s. These values of T_s correspond to $T/T_f=0.9$ and 0.7 for both samples, where T_f is the freezing temperature (Ref. 75). Filled symbols are used to represent the curves measured on cooling, and open symbols the curves measured on heating. The reference curves (without stops) are shown as lines; the arrows indicate the cooling respective of the heating curve. The insets show the difference plots for double-stop experiments (open symbols) and associated single-stop experiments (lines) measured on heating. $\omega/2\pi=510$ mHz and $v_{\text{cool}}^{\text{eff}}\approx v_{\text{heat}}^{\text{eff}}\sim 0.005$.

duced in the susceptibility curves on reheating as seen in the main frames and illustrated as difference plots in the insets of Fig. 20. These figures illustrate one more marked differences in the behavior of the two samples: the memory dips are wider for the $Fe_{0.5}Mn_{0.5}TiO_3$ than for the Ag(11 at% Mn) sample.

B. ZFC memory

ZFC-memory experiments[60,76] will here be used to further elucidate the differences between the two samples. Results of single-stop ZFC memory experiments for the Ag(11 at% Mn) and $Fe_{0.5}Mn_{0.5}TiO_3$ spin glasses are shown in Fig. 21. In both cases, the sample is cooled in zero magnetic field and the cooling is temporary stopped at $T_s/T_f=0.8$ for $t_s=3000$ s (main frame). Here T_f is the freezing temperature of the ZFC magnetization.[75] The cooling is subsequently resumed, and the ZFC magnetization recorded on reheating in

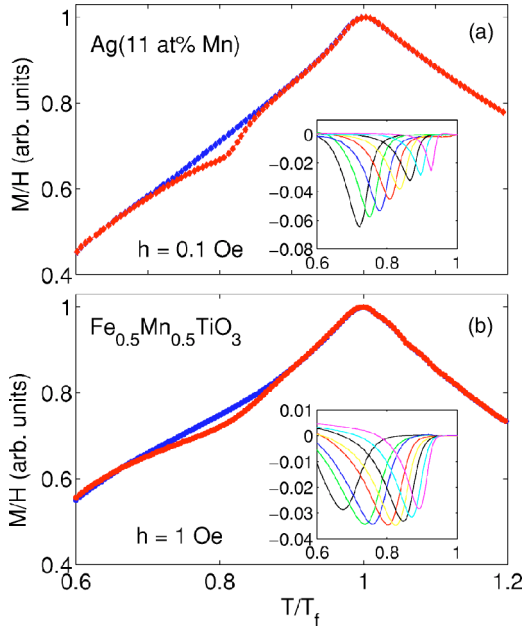

FIG. 21. (Color online) ZFC susceptibility versus T/T_f for (a) the Ag(11 at% Mn) sample and (b) the $Fe_{0.5}Mn_{0.5}TiO_3$ sample. The ZFC susceptibility is measured after continuous cooling (filled symbols) and cooling with a temporary stop (open symbols) of 3000 s at $T_s/T_f\sim 0.8$ ($T_s=27$ K for Ag(11 at% Mn) and $T_s=19$ K for $Fe_{0.5}Mn_{0.5}TiO_3$). The insets show the corresponding difference plots ("stop curve"—reference curve), and additional results for 3000 s stops made at (a) $T_s=24$–31 K and (b) $T_s=16$–21 K. $v_{\text{cool}}\sim 0.05$ K/s and $v_{\text{heat}}^{\text{eff}}\sim 0.005$.

a small magnetic field. A reference curve measured using the same protocol, but without the stop is also recorded. The difference between corresponding reference and single memory curves are plotted in the inset, together with results obtained from similar measurements with stops at some other temperatures. As seen in the main frames, the curves corresponding to the single stops lie significantly below their reference curves in a limited temperature range around T_s/T_f. In the associated difference plots, this appears as "dips" of finite width around the stop temperatures. It has been argued that such dips directly reflect the memory phenomenon.[60]

The memory dips appear much broader for the $Fe_{0.5}Mn_{0.5}TiO_3$ sample than for the Ag(11 at% Mn) sample. This can be seen even more clearly in the double-stop dc-memory experiments shown in Fig. 22. Two 3000 s stops are performed at $T_{s_1}/T_f=0.9$ and $T_{s_2}/T_f=0.72$ during the cooling to the lowest temperature. The results of the corresponding single-stop experiments at T_{s_1} and T_{s_2} are included. For both systems, the sum of the two single-stop curves (not shown here) is nearly equal to the double-stop curve.[76] But, while for Ag(11 at% Mn) the two peaks are well separated, for the same separation in T/T_f, the single-stop curves of $Fe_{0.5}Mn_{0.5}TiO_3$ overlap, due to the larger width of the memory dips.

C. Accumulative versus chaotic processes

In the ghost domain picture, the size of domains at a given temperature T can be increased by aging at nearby tempera-

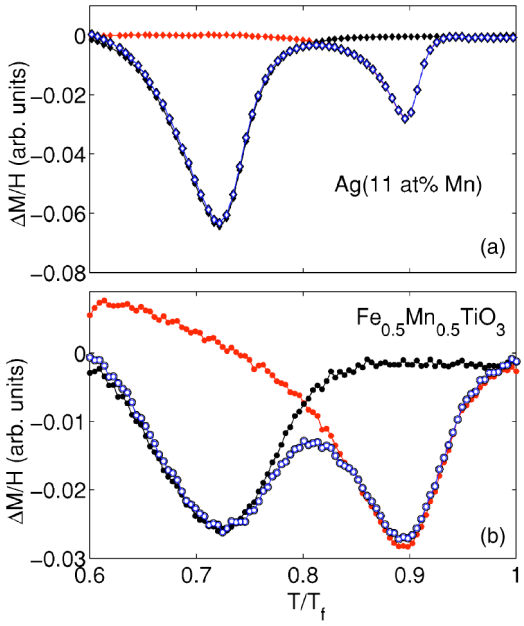

FIG. 22. (Color online) Difference plots of ZFC susceptibility versus T/T_f corresponding to single- and double-stop experiments, with one (or two) temporary stops for 3000 s at (a) $T_{s_1}=30$ K and/or $T_{s_2}=24$ K and (b) $T_{s_1}=21$ K and/or $T_{s_2}=17$ K. The single-stop experiments are represented using filled markers, while open markers are used to represent the double-stop experiments. $v_{\text{cool}} \sim 0.05$ K/s and $v_{\text{heat}}^{\text{eff}} \sim 0.005$.

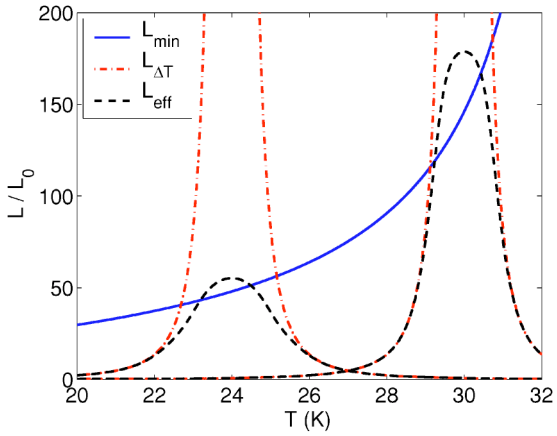

FIG. 23. (Color online) A schematic illustration of the length scales explored in the Ag(11 at% Mn) sample by continuous cooling (and heating) with temporary halts at $T_{s_1}=30$ K and $T_{s_2}=24$ K for $t_{s_1}=t_{s_2}=10^4$ s. The effective domain size grown during the temporary halts at T_s for a time t_s is given by $L_{\text{eff}}=L_{\Delta T=|T-T_s|}F(L_{T_s}(t_s)/L_{\Delta T=|T-T_s|})$ [Eqs. (9)–(12)]. It is bounded from above by the overlap length $L_{\Delta T=|T-T_s|}$. The scaling function $F(x)=\tanh(x)[1-cx^{2\zeta}/\cosh(x)]$ interpolates between the fit to the weakly perturbed regime (shown in Fig. 10) and the strongly perturbed regime $\lim_{x\to\infty}F(x)=1$. Here all parameters for the growth law $L_T(t)$ [see Fig. 24] and the overlap length $L_{\Delta T}$ are the same as in Sec. IV A 4. The continuous cooling and heating yields the minimum effective domain size $L_{\min}$ at all temperatures. Here it is simply assumed to be $L_{\min}=L_T(t_{\min})$ with $t_{\min}=100$ s (Ref. 77).

tures (see Fig. 3). However, noise is induced on the domains at T by the growth of domains at other temperatures outside the overlap region (cf. Sec. II E 2). In particular, the spin configuration subjected to continuous temperature changes with a certain rate v_T is expected to attain a domain size $L_{\min}(v_T,T)$ at temperature T, due to the competition between accumulative aging and chaotic rejuvenation processes (as discussed in Sec. II F). $L_{\min}(v_T,T)$ is reflected on the magnetic response of the systems under continuous temperature changes; the larger $L_{\min}(v_T,T)$, the smaller $\chi''(T)$. In the data of the ac susceptibility measured under continuous cooling and reheating shown in Fig. 20, we found that for the Ag(11 at% Mn) sample the $\chi''(T)$ curve on reheating lies above the one measured on cooling, while the opposite applies to the $Fe_{0.5}Mn_{0.5}TiO_3$ sample. These features suggest strong chaotic rejuvenation in Ag(11 at% Mn) and are much weaker in the $Fe_{0.5}Mn_{0.5}TiO_3$ sample. This is qualitatively consistent with the observations made in the temperature-shift experiments presented in Sec. IV A that the overlap length for the Ag(11 at% Mn) decays faster with increasing ΔT than that of the $Fe_{0.5}Mn_{0.5}TiO_3$ system.

D. An apparent hierarchy of temperatures

In a memory experiment, during a stop made at T_s for a time t_s, the size of the domains becomes $L_{T_s}(t_s)$. The ghost domains at nearby temperatures will also grow but only up to L_{eff} [Eq. (9)], as illustrated in Fig. 23. The $\min[L_{T_s}(t_w),L_{\Delta T=|T_s-T|}]$ is the upper bound for L_{eff}. When the cooling is resumed, the ac-susceptibility curve merges with the reference curve because the overlap length becomes smaller than the minimum domain size $L_{\min}$, which depends on the cooling rate.[77] On subsequent reheating, the domain sizes at the temperatures around T_s are larger than $L_{\min}$ so that the susceptibility curve (ac or dc) measured on heating makes a "dip" with respect to the reference curve without any stop.

Let us compare the schematic picture of length scales for the Ag(11 at% Mn) sample shown in Fig. 23 with the corresponding two-stop memory experiment shown in Figs. 20 and 22. We can see that the widths of the dips around T_s in the memory experiment correspond roughly to the widths of the temperature-profile of the effective domain size L_{eff} at around T_s. The width of the memory dips becomes broader at lower temperatures for all memory experiments both for the Ag(11 at% Mn) and $Fe_{0.5}Mn_{0.5}TiO_3$ samples. In the length scale picture it is also seen that the temperature profile of L_{eff} around T_s becomes broader at lower temperature, due to the temperature dependence of the growth law (see Fig. 24). From this scenario it is clear that a larger overlap length makes the weak chaos regime larger and, hence, the memory dips broader. The observed differences between the width of the dips of the $Fe_{0.5}Mn_{0.5}TiO_3$ and Ag(11 at% Mn) samples may be attributed to such a difference in overlap length in consistency with the results shown in Fig. 9.

The distinct multiple memories shown in Figs. 20 and 22 could suggest some sort of "hierarchy of temperatures." However, it is not necessary to invoke either the traditional hierarchical phase space picture[44] or the hierarchical length scale picture[5,23,26,41–43,55] to understand this multiple-memory

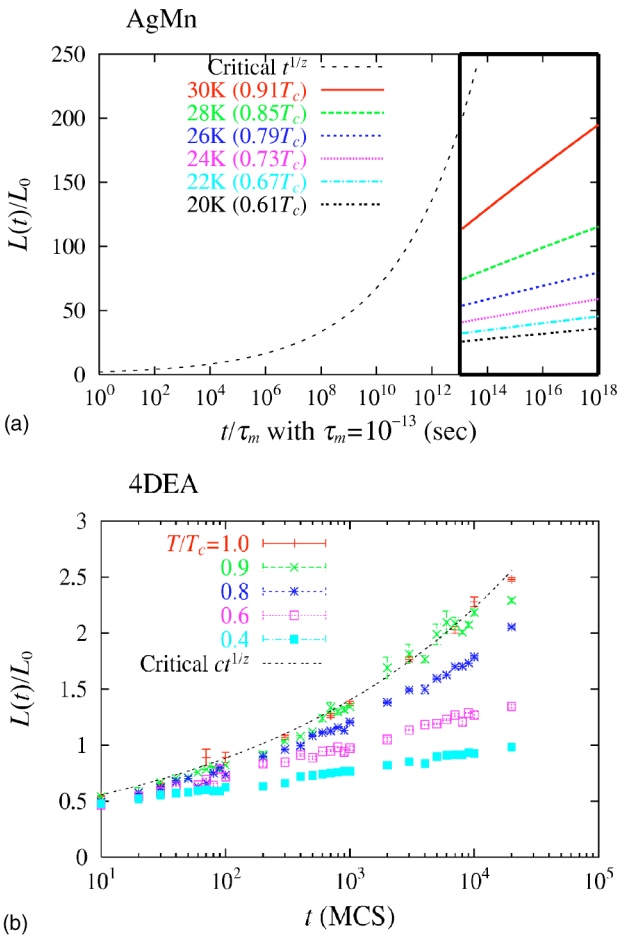

FIG. 24. (Color online) The dynamical length scales relevant in our experiments and simulations. (a) A plot of the growth law [Eq. (A2)] with parameters determined for a Ag(11 at% Mn) sample in Ref. 29 from a scaling analysis of the relaxation of the ac susceptibility in isothermal aging in the range of 20–30 K. The growth law at the critical temperature $L(t)/L_0=(t/\tau_m)^{1/z}$ ($z=6.5$) is also shown. [The possible $O(1)$ prefactor in front of Eq. (A2) and the critical growth law are not known.] The unit of time is chosen to be $\tau_m \sim \hbar/J \sim 10^{-13}$ s. The experimental time and/or length scale is the area surrounded by the box. (b) The size of the domains of a 4D EA Ising spin-glass model determined directly in a previous numerical simulation (Ref. 69), monitoring the spatial correlation function between two real replicas undergoing isothermal aging. The dotted line is the power law for the critical regime $L(t)/L_0=(t/\tau_m)^{1/z}$ with $z=4.98$.

effect. Indeed, the domain sizes grown at the two stop temperatures are almost of the same order of magnitude because thermally activated dynamics does not allow significant hierarchy of length scales explored at different temperatures (as discussed in Appendix A). Thus the scenarios of the memory effect, which strongly relies on the assumption of hierarchy of length scales,[5,23,26,41–43,55] cannot explain the distinct memory dips. Without temperature chaos, the temperature profile of $L_{\rm eff}$ becomes so broad that the memory dips strongly overlap. Our estimates suggest that the sizes of domains, grown at the two stop temperatures shown in Fig. 23, are much larger than the overlap length between the equilibrium spin configurations at the two temperatures within the experimental time scales. Thus the memories imprinted at the two stop temperatures are significantly different from each other. Also, retrieval of such memories under a strong temperature-chaos effect is possible within the ghost domain picture as discussed in Sec. II E. A crucial ingredient in experiments is the finiteness of the heating and cooling rate, which yields the characteristic length scale $L_{\rm min}$, schematically shown in Fig. 23. As discussed in Sec. II F, $L_{\rm min}$ plays the role of a renormalized overlap length, which leads to substantial reductions of the recovery times of memories.

It should, however, be noted that much broader memory dips are observed in experimental systems, such as superspin glasses, for which experiments probe short time (length) scales so that the effect of temperature chaos is negligible, and the memory dip is determined by freezing of smaller and smaller domains on cooling in a fixed-energy landscape[78] (see also Ref. 23). Finally, we note that the width of the memory dips give an indication of the strength of the temperature-chaos effect, but a better estimation is given by the twin T-shift experiments discussed in Sec. IV.

VII. SUMMARY AND CONCLUSION

Rejuvenation (chaos) and memory effects have been investigated after temperature perturbations in two model spin-glass samples, the $Fe_{0.5}Mn_{0.5}TiO_3$ Ising system and the Ag(11 at% Mn) Heisenberg system, as well as after bond perturbations in the four-dimensional EA Ising model. These effects are discussed in terms of the ghost domain picture presented in Sec. II.

- The ZFC relaxation is measured after a T shift for the $Fe_{0.5}Mn_{0.5}TiO_3$ and Ag(11 at% Mn) samples. By analyzing the peak positions of the relaxation rate $S(t)$ using the twin T-shift protocol introduced in Ref. 28, evidence of both accumulative and nonaccumulative aging regimes in both samples were found (cf. Fig. 9). The Ag(11 at% Mn) sample was found to exhibit stronger deviations from fully accumulative aging with increasing $|\Delta T|/T_g$ than the $Fe_{0.5}Mn_{0.5}TiO_3$ sample. A scaling analysis performed on the data of the Ag(11 at% Mn) sample (Fig. 10) reveals increasing rejuvenation effects with increasing ΔT. These rejuvenation effects can consistently be understood in terms of partial chaos at length scales smaller than the overlap length $L_{\Delta T}$, as first proposed in Ref. 30. However, data derived using larger perturbations $|\Delta T|>0.6$ K could not be used in the scaling analysis because the rejuvenation effect saturates due to the slow cooling and/or heating rates. This suggests the emergence of the strongly perturbed regime in the sense that $L_{\Delta T}<L_{\rm min}$, where $L_{\rm min}$ is the smallest observable domain size due to the slow cooling and/or heating. The overlap length can never be directly observed in experiments because it is hidden behind $L_{\rm min}$, as can be seen in the schematic Fig. 23. On the other hand, some properties of the overlap length are obtained indirectly by the scaling in the weakly perturbed regime (Fig. 10).
- In the case of bond-shift simulations, the relaxation rate $S(t)$ is found to show a similar behavior as in the T-shift experiments as shown in Fig. 11; $S(t)$ is initially broadened with increasing strength of the perturbation p, where also the

scaling analysis presented in Fig. 12 exhibits the emergence of corrections to the fully accumulative aging. The scaling ansatz Eqs. (9)–(11) was shown to hold with only the chaos exponent ζ being a fitting parameter; a result that also gives further support to the corresponding analysis from *T*-cycling experiments. However, again the data with stronger perturbation (larger p) could not be used in the scaling because the peak positions saturated to $O(1)$ (MCS), which is the minimum time scale. In such a regime, $S(t)$ exhibits considerable narrowing with the peak at $O(1)$ (MCS). This can again be understood to be due to the emergence of the strongly perturbed regime in the sense that $L_{\Delta T} \sim L_0$, where L_0 is the unit of lattice spacing.

• For the Ag(11 at% Mn) sample, temperature changes $|\Delta T| \gtrsim 1$ K were shown to cause strong perturbations to the system. One- and two-step negative *T*-cycling protocols were used in order to investigate the healing after such strong perturbations. The recovery times after one-step cyclings shown in Figs. 14 and 15 were found to be anomalously larger than the trivial recovery times $t_{\rm rec}^{\rm weak}$ given in Eq. (15) (which could be evaluated using the growth law confirmed in Sec. IV A 4). Furthermore, the two-step cyclings data displayed in Fig. 17 show that the effects of perturbations made at two different temperatures can give rise to much stronger rejuvenation than only an additive increase of the effects of single perturbations. These striking features are in agreement with ghost domain scenario (Sec. II E).

• In the bond-cycling simulations, a large strength of the perturbation, $p=0.2$ was used to focus on the strongly perturbed regime. The healing process after one-step cycling simulations displayed in Fig. 18 and the two-step bond cycling shown in Fig. 19 were found to require anomalously large recovery times, in consistency with the results from *T*-cycling experiments and the predictions of the ghost domain scenario. It is also demonstrated in Fig. 19 that a "memory" of the history before the perturbation cannot be erased completely even if the duration of the perturbation is effectively longer than the duration of the preceding history.

• It is proposed that the effects of finite heating and/or cooling rates v_T can be parametrized by a renormalized overlap length $L_{\rm min}(v_T, T)$. In combination with a strong separation of time scales, this can lead to an apparent "hierarchy of temperatures," as has been suggested earlier from experimental observations, e.g., in Refs. 79 and 80. In the ghost domain scenario, however, the temperature chaos effect is the mechanism that allows distinctness of memories at each level of the "hierarchy" as illustrated in Fig. 23. This explains the two well-separated memory dips seen in the memory experiment shown in Fig. 20, for example.

To conclude, dynamical properties of the Ising $Fe_{0.5}Mn_{0.5}TiO_3$ and the Heisenberg Ag(11 at% Mn) spin glasses subjected to temperature changes and the four-dimensional Edwards-Anderson Ising spin-glass model subjected to bond changes are examined and compared to each other in detail. The temperature-shift and cycling experiments and bond-shift and cycling simulations show remarkably similar features suggesting a common mechanism of the rejuvenation and memory effects. The detailed features of the rejuvenation effects after temperature and bond shifts are found to agree with the anticipated crossover from weakly to strongly perturbed regimes of the chaos effects. Quantitative differences in different systems can be attributed to differences of the magnitude of the overlap length. Anomalously large recovery times of the memories are found to be required in the one- and two-step temperature and bond cycling experiments when performed into the strongly perturbed regime, in agreement with the ghost domain scenario.

ACKNOWLEDGMENTS

We thank Jean-Philippe Bouchaud, Ian Campbell, Koji Hukushima, Hikaru Kawamura, Philipp Maas, Falk Scheffler, Tetsuya Sato, Hajime Takayama, and Eric Vincent for stimulating discussions. This work was financially supported by the Swedish Research Council (VR). H.Y. is supported by the Ministry of Education, Culture, Sports, Science and Technology of Japan, Grant-in-Aid for Scientific Research No. 14740233.

APPENDIX A: SEPARATION OF LENGTH AND TIME SCALE

In this appendix we summarize important properties of activated dynamics that govern the growth of domains in spin glasses. At mesoscopic levels, the dynamics of a spin glass at temperatures below T_g is governed by nucleation of dropletlike excitations.[18] The energy barrier associated with a droplet of size L is assumed to scale as $E_b \sim \Delta(T)(L/L_0)^{\psi}$ with $\psi > 0$. Then the time needed to nucleate a droplet by thermal activation becomes

$$\tau_L(T) = \tau_0(T) \exp\left[\frac{\Delta(T)}{k_B T}\left(\frac{L}{L_0}\right)^{\psi}\right], \tag{A1}$$

where the effects of critical fluctuations are taken into account in a renormalized way in the characteristic energy scale $\Delta(T)$ for the free-energy barrier and the characteristic time scale $\tau_0(T)$ for the thermally activated processes. They scale as $\Delta(T)/J \sim \epsilon^{\psi\nu}$ and $\tau_0(T)/\tau_m \sim [\xi(T)/L_0]^z \sim |\epsilon|^{-z\nu}$ with $\epsilon = T/T_g - 1$. The microscopic time scale is $\tau_m \sim \hbar/J \sim 10^{-13}$ s in atomic spin glasses and one Monte Carlo step (MCS) in Monte Carlo simulations. $J \sim T_g$ sets the energy unit, z is the dynamical critical exponent, and ν the exponent for the divergence of the correlation length. The importance of accounting for critical fluctuations has been realized in analyses of recent simulations[26,63,69] and experiments.[23,29]

From Eq. (A1) it follows that within a time scale t, a droplet excitation as large as

$$L_T(t) \sim L_0\left[\frac{k_B T}{\Delta(T)} \ln\left(\frac{t}{\tau_0(T)}\right)\right]^{1/\psi} \tag{A2}$$

can be thermally activated. At finite time scales there must be corrections to the asymptotic form Eq. (A2) due to critical fluctuations[23,63] as well as logarithmic correction terms to the energy barriers,[81] but the actual forms of the corrections are not yet known in spin glasses.

An immediate consequence of activated dynamics is an extremely wide separation of time scales with temperature. On the other hand, the variation of length scales with tem-

perature is very mild (typically less than one order of magnitude). Let us consider two arbitrarily close temperatures T and $T+\Delta T$. From Eq. (A1) it follows that the ratio of time scales at the two temperatures associated with a given length L for $\Delta T/T \ll 1$ becomes

$$\frac{\tau_L(T)}{\tau_L(T+\Delta T)} \sim \frac{\tau_0(T)}{\tau_0(T+\Delta T)} \exp\left[\left(\frac{L}{L_*(\Delta T)}\right)^{\psi}\right], \quad \text{(A3)}$$

where we introduced *time-separation length*

$$L_*(\Delta) \sim L_0 |(\partial(\Delta(T)/k_B T)/\partial T)\Delta T|^{-1/\psi}. \quad \text{(A4)}$$

The above expression means that two times become *exponentially* separated if one observes dynamics on length scales large enough compared to the time-separation length $L_*(\Delta T)$. Note that $L_*(\Delta T)$ remains finite as long as ΔT is nonzero. Looking at the ratio of length scales for a given time scale t at the two temperatures one finds from Eq. (A2),

$$\frac{L_{T+\Delta T}(t)}{L_T(t)} \sim O(1) \quad \text{(A5)}$$

independently of the chosen time scale t. Thus, the magnitude of the length scales explored at two close temperatures appears quite similar as long as the same time scales are used. However, we emphasize that thermally activated dynamics brings about a significant hierarchy of time scales, in spite of an apparent mild hierarchy in length scales.

Assuming that Eq. (A2) is applicable to the Heisenberg-like Ag(11 at% Mn) spin glass, Fig. 24(a) shows the domain growth at different temperatures in this system using earlier derived experimental values for the parameters.[29] In Fig. 24(b) the domain growth at different temperatures is drawn for a 4D EA spin glass derived from previous numerical simulations.[69]

In spin-glass materials the microscopic time is $\tau_m \sim 10^{-13}$ s and relaxation experiments are performed typically in the range of time scales $1-10^5$ s or $t/\tau_m = 10^{13}-10^{18}$. On the other hand, in usual Monte Carlo simulations of EA Ising spin-glass models, the microscopic time is $\tau_m = 1$ MCS and the range of time scales is $1-10^6$ MCS or $t/\tau_m = 1-10^6$. Because of the slow dynamics, there is a common problem that the investigated four to six decades in time only cover a quite limited length scale as shown in Fig. 24 (see also Fig. 1 of Ref. 26). Due to the much shorter time scales probed in numerical simulations, the influence of critical dynamics are much stronger than in experiments for the same reduced temperature T/T_g. It can also be seen in Fig. 24 that the length scales are rather different: simulations explore length scales of order $L_T(t)/L_0 \sim O(1)$ while experiments explore $L_T(t)/L_0 \sim O(10)-O(10^2)$.

APPENDIX B: EXPERIMENTAL DETAILS

1. 1. Noncommercial SQUID magnetometer

The experiments were performed in noncommercial SQUID magnetometers,[59] designed for low-field measurements and optimum temperature control. The magnetic field is in these setups generated by a small superconducting solenoid always working in persistent mode. The time constant of the superconducting magnets is of order 1 ms, but the whole procedure to change the field from h to $h+\Delta h$ and reestablish persistent mode in the magnet takes ~ 0.3 s, which also determines the shortest observation time in the ZFC-relaxation experiments. In the case of the $Fe_{0.5}Mn_{0.5}TiO_3$ sample, cut into a rectangular shape ($2\times 2\times 4$ mm^3) with the c-axis along the longest side, the probing field was applied along the c-axis of the single crystal, and for the Ag(11 at% Mn) spin glass, turned into a cylindrical shape (4 mm long and 2 mm in diam); the field was applied along the symmetry axis of the cylinder. The sample space is magnetically shielded with cans of μ-metal and niobium and the remaining background field is <1 mOe, while the measurement fields used are $h \approx 0.1-1$ Oe. The sample is glued to a 50 mm long sapphire rod with a diameter of 2 mm, and the magnetization is recorded while keeping the sample stationary in the center of the third coil of a third-order gradiometer. The sapphire rod is connected to a solid copper cylinder on which the thermometer and a resistive heater are placed. The materials in the experimental setup are chosen so that the heat transfer between the sample and copper cylinder is maximized while the heat exchange with the surroundings is kept quite low, being mainly carried by thermal conduction through the sample holder rod—a thin-walled stainless steel tube, via Cu(Be) holding springs into the surrounding helium bath. The temperature can be kept fixed with a stability better than 100 μK using an ac-bridge-based temperature control system and with a stability better than 5 mK using a commercial temperature controller. The maximum cooling rate in these magnetometers is $v_{\text{cool}} \sim 0.05$ K/s in the temperature ranges of these studies and, to maintain a good temperature control, the maximum heating rate is limited to $v_{\text{heat}} \sim 0.5$ K/s. The maximum heating and cooling rates were always employed when changing the temperature in the current experiments. In ac measurements, a coil generating the ac field is wound around the sample and a similar compensation coil is wound on the sample rod above the sample and positioned so that it becomes centered in the second pickup coil of the gradiometer.

When measuring both the ac and dc susceptibility as a function of temperature, the magnetization is recorded on heating by elevating the temperature in steps of 0.1–0.2 K. The measurement of the magnetization at constant temperature (including temperature setting and stabilization, and actual measurement) takes $\sim$30–60 s, yielding an effective heating rate of $v_T^{\text{eff}} \sim 0.005$ K/s. The magnetization is also recorded on cooling in ac experiments yielding a cooling rate similar to the heating rate, while the sample is cooled using the maximum cooling rate in dc experiments.

Since the same thermal protocols are employed in both dc-magnetization and ac-susceptibility measurements, the same nonequilibrium processes are probed in both methods, with the difference that the ac susceptibility can be measured at all times and temperatures during the thermal protocols, while the zero-field cooled (ZFC) magnetization can only be recorded as a function of temperature (respective time) after applying the probing field at the lowest temperature (respective measurement temperature). The magnetic fields em-

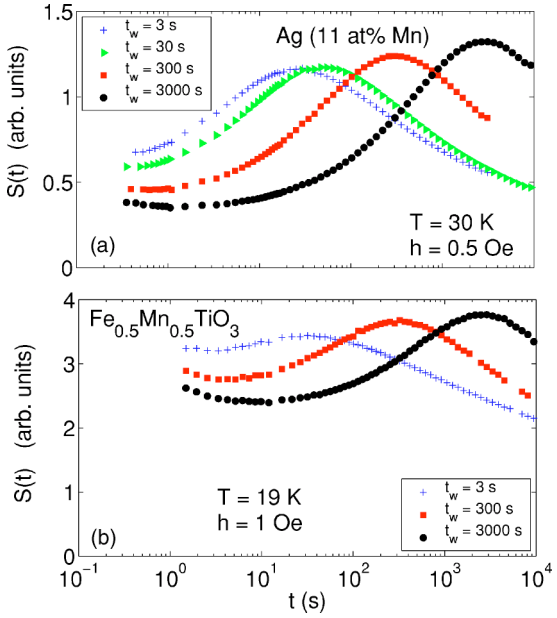

FIG. 25. (Color online) $S(t)$ of ZFC-relaxation measurements employing different wait times on (a) Ag(11 at% Mn) and (b) $Fe_{0.5}Mn_{0.5}TiO_3$. The reduced temperature is 0.9 for both samples.

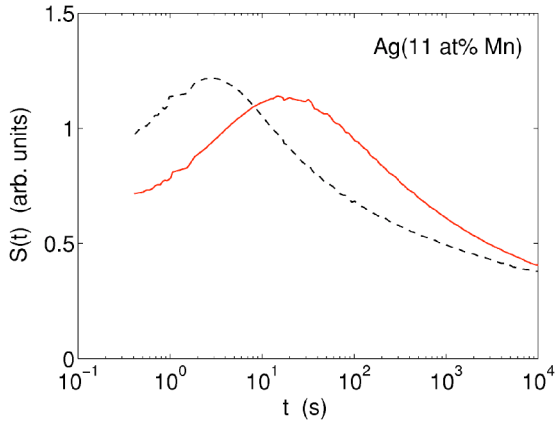

FIG. 26. (Color online) $S(t)$ curves obtained for Ag(11 at% Mn) after a rapid cooling ($v_{\mathrm{cool}} \sim 0.05$ K/s) to $T_m = 30$ K (solid line) and after a rapid cooling to 29 K, where the sample was kept for 3000 s and subsequently heated rapidly ($v_{\mathrm{heat}} \sim 0.5$ K/s) to $T_m = 30$ K (dashed line).

ployed in the experiments are small enough to ensure a linear response of the system, and do hence not affect the nonequilibrium dynamics.

Some complementary magnetization measurements were performed using a Quantum Design MPMS5 SQUID magnetometer in order to check the absolute susceptibility values.

2. 2. Effective age of a spin glass system measured by ZFC relaxation

The relaxation rate $S(t)$ determined from isothermal ZFC-relaxation experiments is shown in Fig. 25. The sample is quenched (cooled with the maximum cooling rate) from above T_g to the measurement temperature T_m. For both samples $S(t)$ exhibits a peak at $t_{\mathrm{peak}} \approx t_w$ except for the shortest waiting time $t_w = t_{ws} = 3$ s (which is the time needed in order to stabilize the temperature[64]). Due to the slow cooling, the system has already been aged for a certain effective time t_{min} when reaching T_m.[82] From the measurements with $t_w = t_{ws}$ we can determine $t_{\mathrm{min}} = t_{\mathrm{peak}} \approx 20-40$ s. The effective age of the system after a T shift is determined from the time t_{peak} corresponding to the maximum of $S(t)$, as $t_{\mathrm{eff}}(t_w + t_{\mathrm{min}}) = (t_{\mathrm{peak}})^{1/\mu}$ with $\mu = 1$ for the Ag(11 at% Mn) sample at $T \approx 30$ K and $\mu \approx 0.98$–0.99 at $T = 17$–19 K for the $Fe_{0.5}Mn_{0.5}TiO_3$ sample.[83] We notice that t_{min} can only be determined from isothermal ZFC-relaxation measurements, but not from the corresponding ac-relaxation measurement.

In Fig. 26, $S(t)$ is shown after a temperature quench ($v_{\mathrm{cool}} \sim 0.05$ K/s) to T_m and after a T shift to a temperature $T_i = 29$ K, where it is aged for 3000 s before the temperature is rapidly raised ($v_{\mathrm{heat}} \sim 0.5$ K/s) to T_m. The maximum of the $S(t)$ curve of the T-shift experiment appears at $t_{\mathrm{min}} \sim 3$ s, which is a considerably shorter time than $t_{\mathrm{min}} \sim 30$ s in the case of quench. The fact that t_{min} is smaller after a positive T shift than after a direct quench implies that the system is completely dominated by the strong chaos effect. Namely, $|\Delta T|$ is so large that the intrinsic overlap length $L_{\Delta T} < L_{\mathrm{min}}$, where L_{min} is the domain size corresponding to the effective age t_{min}. We cannot evaluate the value of $L_{\Delta T}$ itself because it is masked by L_{min} (on heating). $t_{\mathrm{min}}(L_{\mathrm{min}})$ is smaller on heating than on cooling due to the faster heating than cooling rate and the temperature dependence of the domain growth (cf. Appendix A). The L_{min} corresponding to t_{min} determined here gives an upper limit for the renormalized overlap length $L_{\mathrm{min}}(v_T, T)$ introduced in Sec. II F because the time needed to stabilize the temperature at T_m also contributes to $t_{\mathrm{min}}(L_{\mathrm{min}})$. It is also possible to obtain a random initial configuration with a small t_{min} by using a magnetic field making a "field quench."[84] Throughout this article, we have, however, only used the ordinary temperature quench to initialize the system.

APPENDIX C: SIMULATIONAL DETAILS

The Monte Carlo simulations were performed on the four-dimensional EA Ising model whose critical temperature is $T_g/J = 2.0$ (Ref. 61). The simulations were made at the temperatures $T/J = 1.2, 0.8$ ($T/T_g = 0.6, 0.4$), which are well below the critical temperature so that numerical time and length scales are *not* strongly affected by critical fluctuations. Systems with 24^4 spins were used, which are large enough to get rid of finite size effects within the numerical time window.[63] The simulations were done using the standard heat-bath Monte Carlo method up to a time scale of 10^5 MCS, starting with random spin configurations in order to mimic aging after ideal temperature quenches. The average over at least 32 different realizations of random bonds were taken. For the measurements of the ZFC susceptibilities, 320 samples were used.

The advantage of the four-dimensional model compared

with the three-dimensional EA-Ising model, which might appear slightly more realistic, is that a rich amount of knowledge about the equilibrium and dynamical properties of the model has been accumulated by independent studies. This includes the critical properties associated with the fixed point at T_g,[61] the $T=0$ glassy fixed point,[85,86] and the dynamical length $L_T(t)$ obtained in Refs. 63 and 69. We note that a recent Monte Carlo simulation[63] on the same model confirmed, to a certain extent, certain predictions from the fundamental dynamical scaling ansatz due to the droplet theory[16–18] [including that for the decay of TRM (thermoremanent magnetization)], which are all expressed in terms of the dynamical length scale $L_T(t)$. It is also worth mentioning that in equilibrium Monte Carlo simulations of the model, the anticipated signatures of the chaos effect have been observed both in the case of temperature changes[71] (exchange Monte Carlo method) and bond perturbation.[37]

Unfortunately, within the available computational power it is difficult to observe even some weak traces of rejuvenation by temperature changes by the standard heat-bath dynamical Monte Carlo simulations.[25,26,39,41,42,87] Within feasible CPU times, one is forced to work at temperatures rather close to T_g, such as $0.8–0.9T_g$. In this temperature range, the dynamics in the numerical time window is strongly affected by critical fluctuations,[26,30,63,69] while the experimental time window lies well outside the critical regime[30] (see Fig. 24). Thus we limit ourselves with bond-shift and cycling simulations.

*Present address: RIKEN, Hirosawa 2-1, Wako, Saitama 351-0198, Japan. Electronic address: pjonsson@riken.jp

†Present address: ERATO-SSS/JST, Cryogenic Center, University of Tokyo, 2-11-16 Yayoi, Bunkyo-ku, Tokyo 113-0032, Japan.

[1] V. Cannella and J. A. Mydosh, Phys. Rev. B **6**, 4220 (1972).
[2] S. F. Edwards and P. W. Anderson, J. Phys. F: Met. Phys. **5**, 965 (1975).
[3] D. Sherrington and S. Kirkpatrick, Phys. Rev. Lett. **35**, 1792 (1975).
[4] J.-P. Bouchaud, L. F. Cugliandolo, J. Kurchan, and M. Mézard, in *Spin Glasses and Random Fields*, edited by A. P. Young (World Scientific, Singapore, 1997), pp. 161–223.
[5] J.-P. Bouchaud, in *Soft and Fragile Matter*, edited by M. E. Cates and M. R. Evans (IOP, Bristol, 2000).
[6] L. Lundgren, P. Svedlindh, P. Nordblad, and O. Beckman, Phys. Rev. Lett. **51**, 911 (1983).
[7] K. Jonason, E. Vincent, J. Hammann, J.-P. Bouchaud, and P. Nordblad, Phys. Rev. Lett. **81**, 3243 (1998).
[8] T. Jonsson, K. Jonason, P. Jönsson, and P. Nordblad, Phys. Rev. B **59**, 8770 (1999).
[9] P. Doussineau, T. de Lacerda-Arôso, and A. Levelut, Europhys. Lett. **46**, 401 (1999).
[10] L. Bellon, S. Ciliberto, and C. Laroche, Europhys. Lett. **51**, 551 (2000).
[11] H. Mamiya, I. Nakatani, and T. Furubayashi, Phys. Rev. Lett. **82**, 4332 (1999).
[12] P. Jönsson, M. F. Hansen, and P. Nordblad, Phys. Rev. B **61**, 1261 (2000).
[13] R. Mathieu, P. Svedlindh, and P. Nordblad, Europhys. Lett. **52**, 441 (2000).
[14] E. L. Papadopoulou, P. Nordblad, P. Svedlindh, R. Schöneberger, and R. Gross, Phys. Rev. Lett. **82**, 173 (1999).
[15] A. Gardchareon, R. Mathieu, P. E. Jönsson, and P. Nordblad, Phys. Rev. B **67**, 052505 (2003).
[16] A. J. Bray and M. A. Moore, Phys. Rev. Lett. **58**, 57 (1987).
[17] D. S. Fisher and D. A. Huse, Phys. Rev. B **38**, 386 (1988).
[18] D. S. Fisher and D. A. Huse, Phys. Rev. B **38**, 373 (1988).
[19] D. S. Fisher and D. A. Huse, Phys. Rev. B **43**, 10 728 (1991).
[20] H. Yoshino, A. Lemaître, and J.-P. Bouchaud, Eur. Phys. J. B **20**, 367 (2001).
[21] F. Scheffler, H. Yoshino, and P. Maass, Phys. Rev. B **68**, 060404(R) (2003).
[22] H. Yoshino, J. Phys. A **36**, 10819 (2003).
[23] J.-P. Bouchaud, V. Dupuis, J. Hammann, and E. Vincent, Phys. Rev. B **65**, 024439 (2002).
[24] V. Dupuis, E. Vincent, J.-P. Bouchaud, J. Hammann, A. Ito, and H. A. Katori, Phys. Rev. B **64**, 174204 (2001).
[25] L. Berthier and J. P. Bouchaud, Phys. Rev. Lett. **90**, 059701 (2003).
[26] L. Berthier and J. P. Bouchaud, Phys. Rev. B **66**, 054404 (2002).
[27] A. J. Kovacs, Fortschr. Hochpolym.-Forsch. **3**, 394 (1963).
[28] P. E. Jönsson, H. Yoshino, and P. Nordblad, Phys. Rev. Lett. **89**, 097201 (2002).
[29] P. E. Jönsson, H. Yoshino, P. Nordblad, H. Aruga Katori, and A. Ito, Phys. Rev. Lett. **88**, 257204 (2002).
[30] P. E. Jönsson, H. Yoshino, and P. Nordblad, Phys. Rev. Lett. **90**, 059702 (2003).
[31] J. R. Banavar and A. J. Bray, Phys. Rev. B **35**, 8888 (1987).
[32] M. Ney-Nifle and H. J. Hilhorst, Physica A **193**, 48 (1993).
[33] T. Aspelmeier, A. J. Bray, and M. A. Moore, Phys. Rev. Lett. **89**, 197202 (2002).
[34] T. Rizzo and A. Crisanti, Phys. Rev. Lett. **90**, 137201 (2003).
[35] M. Sales and H. Yoshino, Phys. Rev. E **65**, 066131 (2002).
[36] F. Ritort, Phys. Rev. B **50**, 6844 (1994).
[37] M. Ney-Nifle, Phys. Rev. B **57**, 492 (1998).
[38] A. Billoire and E. Marinari, J. Phys. A **33**, L265 (2000).
[39] M. Picco, F. Ricci-Tersenghi, and F. Ritort, Phys. Rev. B **63**, 174412 (2001).
[40] A. Billoire and E. Marinari, Europhys. Lett. **60**, 775 (2002).
[41] H. Takayama and K. Hukushima, J. Phys. Soc. Jpn. **71**, 3003 (2002).
[42] T. Komori, H. Yoshino, and H. Takayama, J. Phys. Soc. Jpn. **69** Suppl. A, 228 (2000).
[43] L. Berthier and P. C. W. Holdsworth, Europhys. Lett. **58**, 35 (2002).
[44] E. Vincent, J. Hammann, M. Ocio, J.-P. Bouchaud, and L. F. Cugliandolo, in *Complex Behaviour of Glassy Systems: Proceedings of the XIV Sitges Conference*, edited by E. Rubi (Springer, Berlin, 1996).
[45] G. J. M. Koper and H. J. Hilhorst, J. Phys. (Paris) **49**, 429 (1988).
[46] J. Houdayer and O. C. Martin, Europhys. Lett. **49**, 794 (2000).
[47] F. Krzakala and O. C. Martin, Phys. Rev. Lett. **85**, 3013 (2000).

[48] M. Palassini and A. P. Young, Phys. Rev. Lett. **85**, 3017 (2000).
[49] F. Krzakala, Europhys. Lett. **66**, 847 (2004).
[50] Note that in a previous article (Ref. 30) we have proposed the correction term to be $O(p_{\mathrm{minor}})$. However, $O(p_{\mathrm{minor}}^2)$ term seems more natural because L_{eff} should be an even function of ΔT (and ΔJ) and analytic at $\Delta T=0$ (and $\Delta J=0$).
[51] The Mattis model itself does show neither spontaneous bond nor temperature chaos effects. However, it is useful to illustrate and examine the ideas of ghost domains because (i) the model can be designed to have a desired random spin configuration $\{\sigma_i\}$ as its ground state and (ii) the dynamics is unambiguously of the domain growth type. The Hamiltonian is formally given as Eq. (1) but with the coupling given as $J_{ij}=J(1-ar_i)\sigma_i\sigma_j$. The backbone spin configuration of the target equilbrium state is unambiguously given by the ground state, which is $\{\sigma_i\}$. Here a pinning effect is introduced: r_i is a random number, uniformly distributed between 0 and 1, that controls the strength of random pinning, which induces domain growth by thermally activated processes (Ref. 88). The dynamics is simulated by a usual single spin flip heat-bath Monte Carlo algorithm. The procedure of the simulation is as the following. First, the Hamiltonian of a ground state $\{\sigma^A\}$ is applied a time t_w (*initial aging stage*). Then, the Hamiltonian of a different ground state $\{\sigma^B\}$ is applied an additional time τ_p (*perturbation stage*). Finally, the Hamiltonian is set back to the original one, which is applied an additional time τ_h (*healing stage*). The two ground states $\{\sigma^A\}$ and $\{\sigma^B\}$ are chosen to be completely independent from each other to mimic strong chaos with overlap length 1. In Fig. 2, the lattice has $N=400\times 400$ spins. The pinning strength is set $a=0.5$ and temperature is cycled as $T_A\rightarrow T_B\rightarrow T_A$ with $T_A/J=0.2$ and $T_B/J=0.1$. The time steps are chosen as (left figures) $t_w=10^6$, $\tau_p=10^2$, $\tau_h=10^1$ (MCS) and (right figures) $t_w=\tau_p=10^6$, $\tau_h=10^5$ (MCS).
[52] A. J. Bray and J. G. Kissner, J. Phys. A **25**, 31 (1992).
[53] P. Granberg, L. Lundgren, and P. Nordblad, J. Magn. Magn. Mater. **92**, 228 (1990).
[54] R. L. Leheny and S. R. Nagel, Phys. Rev. B **57**, 5154 (1998).
[55] L. Berthier, V. Viasnoff, O. White, V. Orlyanchik, and F. Krzakala (unpublished).
[56] E. Bertin, J.-P. Bouchaud, J.-M. Drouffe, and C. Godreche, J. Phys. A **36**, 10 701 (2003).
[57] A. Ito, H. Aruga, E. Torikai, M. Kikuchi, Y. Syono, and H. Takei, Phys. Rev. Lett. **57**, 483 (1986).
[58] A. Ito, E. Torikai, S. Morimoto, H. Aruga, M. Kikuchi, Y. Syono, and H. Takei, J. Phys. Soc. Jpn. **59**, 829 (1990).
[59] J. Magnusson, C. Djurberg, P. Granberg, and P. Nordblad, Rev. Sci. Instrum. **68**, 3761 (1997).
[60] R. Mathieu, P. Jönsson, D. N. H. Nam, and P. Nordblad, Phys. Rev. B **63**, 092401 (2001).
[61] L. W. Bernardi and I. A. Campbell, Phys. Rev. B **56**, 5271 (1997).
[62] H. Rieger, in *Annual Review of Computational Physics II*, edited by D. Stauffer (World Scientific, Singapore, 1995).
[63] H. Yoshino, K. Hukushima, and H. Takayama, Phys. Rev. B **66**, 064431 (2002).
[64] The noncommercial squid magnetometer used in this study has been designed for fast temperature stabilization, but a sample with good heat conductivity is also essential. Under different experimental conditions, t_{ws} might be much longer, see, e.g., Ref. 89.
[65] P. Granberg, L. Sandlund, P. Nordblad, P. Svedlindh, and L. Lundgren, Phys. Rev. B **38**, 7097 (1988).
[66] L. Sandlund, P. Svedlindh, P. Granberg, P. Nordblad, and L. Lundgren, J. Appl. Phys. **64**, 5616 (1988).
[67] C. Djurberg, K. Jonason, and P. Nordblad, Eur. Phys. J. B **10**, 15 (1999).
[68] D. Hérisson and M. Ocio, Phys. Rev. Lett. **88**, 257202 (2002).
[69] K. Hukushima, H. Yoshino, and H. Takayama, Prog. Theor. Phys. **138**, 568 (2000).
[70] The values of t_{peak} are obtained for $t_w=10,30,100,300,\ldots,10^5$ (MCS) by simulating isothermal aging. Some data are shown in Fig. 11(a). Then t_w is viewed as a function of t_{peak}, and it was fitted to a polynomial of $\log(t_{\mathrm{peak}})$, and the resulting smooth-fitting function was considerd as the model function of $t_w=t_{\mathrm{eff}}(t_{\mathrm{peak}})$.
[71] K. Hukushima and Y. Iba, cond-mat/0207123.
[72] Factors that can affect the estimation of t_{rec} are the noise in the ac signal and the time needed to stabilize the temperature (and the ac signal) after the cycling.
[73] M. Sasaki, V. Dupuis, J.-P. Bouchaud, and E. Vincent, Eur. Phys. J. B **29**, 469 (2002).
[74] L. Bellon, S. Ciliberto, and C. Laroche, Eur. Phys. J. B **25**, 223 (2002).
[75] In ac experiments, it is possible to define a frequency-dependent freezing temperature T_f from a rather sharp maximum in the in-phase component of the susceptibility. Below this temperature, the longest relaxation time of the system exceeds the observation time ($t_{obs}=1/\omega$) employed and a finite out phase component of the susceptibility appears. T_f approaches T_g for low frequencies and increases with increasing frequency. In low-field dc-magnetization measurements, a corresponding maximum is observed in the temperature dependence of the ZFC magnetization. Such an experiment looks at the system on a certain observation time, that by comparison to ac-susceptibility results can be estimated to 10–100 s. By this analogy, we denote this temperature T_f, which was found in our experiments to be equal to 23.6 K for $Fe_{0.5}Mn_{0.5}TiO_3$ and 33.5 K for Ag(11 at% Mn). In the dc memory experiments, the stop temperatures (T_s) were chosen at similar T_s/T_f values for both systems.
[76] R. Mathieu, P. E. Jönsson, P. Nordblad, H. A. Katori, and A. Ito, Phys. Rev. B **65**, 012411 (2002).
[77] In Fig. 23, L_{min} for the continuous cooling and/or heating protocol is for simplicity given as L_T(100 s). This is based on the observation that in an isothermal aging experiment, after temperature quenches down to T_m, we find the effective times $t_{\mathrm{eff}}\approx 30$ s (see Figs. 25 and 7). In memory experiments, the cooling and/or heating rate is lower than the maximum one and we, therefore, expect L_{min} to be a bit larger. The exact value of L_{min} are different on cooling and heating as discussed in Sec. VI C.
[78] P. E. Jönsson, H. Yoshino, H. Mamiya, and H. Takayama, cond-mat/0405276.
[79] M. Lederman, R. Orbach, J. M. Hammann, M. Ocio, and E. Vincent, Phys. Rev. B **44**, 7403 (1991).
[80] F. Lefloch, J. Hammann, M. Ocio, and E. Vincent, Europhys. Lett. **18**, 647 (1992).
[81] L. V. Mikheev, B. Drossel, and M. Kardar, Phys. Rev. Lett. **75**, 1170 (1995).
[82] G. F. Rodriguez, G. G. Kenning, and R. Orbach, Phys. Rev. Lett. **91**, 037203 (2003).
[83] The values of μ were determined from isothermal ZFC-relaxation experiments, where $t_{\mathrm{peak}}=(t_w+t_{\mathrm{min}})^{\mu}$.

[84] P. Nordblad, P. Svedlindh, P. Granberg, and L. Lundgren, Phys. Rev. B **35**, 7150 (1987).
[85] K. Hukushima, Phys. Rev. E **60**, 3606 (1999).
[86] A. K. Hartmann, Phys. Rev. E **59**, 84 (1999).
[87] H. Rieger, J. Phys. I **4**, 883 (1994).
[88] D. A. Huse and C. L. Henley, Phys. Rev. Lett. **54**, 2708 (1985).
[89] F. Bert, V. Dupuis, E. Vincent, J. Hammann, and J.-P. Bouchaud, Phys. Rev. Lett. **92**, 167203 (2004).